

The Nuclear Starburst in NGC 253

C. W. Engelbracht, M. J. Rieke, G. H. Rieke
Steward Observatory, University of Arizona, Tucson, AZ 85721

D. M. Kelly
Wyoming Infrared Observatory, University of Wyoming, Laramie, WY 82071

and

J. M. Achtermann^{1,2}
Department of Astronomy/McDonald Observatory, University of Texas, Austin, TX 78712

ABSTRACT

We have obtained long-slit spectra of NGC 253 in the J, H, K, and N bands, broadband images in the J, H, and K_s bands, narrowband images centered at the wavelengths of $\text{Br}\gamma$ and $\text{H}_2(1,0)\text{S}(1)$, and imaging spectroscopy centered on $[\text{Ne II}](12.8\mu\text{m})$. We have subtracted a composite stellar spectrum from the galaxy spectrum to measure faint emission lines which otherwise would be buried in the complicated continuum structure.

We use these data and data from the literature in a comprehensive re-assessment of the starburst in this galaxy. We confirm that the $[\text{Fe II}]$ emission is predominantly excited by supernova explosions and show that the rate of these events can be derived from the strength of the infrared $[\text{Fe II}]$ lines. Although the H_2 emission superficially resembles a thermally excited spectrum, most of the H_2 infrared luminosity is excited by fluorescence in low density gas. We confirm the presence of a bar and also show that this galaxy has a circumnuclear ring. The relation of these features to the gaseous bar seen in CO is in agreement with the general theoretical picture of how gas can be concentrated into galaxy centers by bars. We derive a strong upper limit of $\sim 37,000\text{K}$ for the stars exciting the emission lines. We use velocity-resolved infrared spectra to determine the mass in the starburst region. Most of this mass appears to be locked up in the old, pre-existing stellar population. Using these constraints and others to build an evolutionary synthesis model, we find that the IMF originally derived to fit the starburst in M 82 also accounts for the properties of NGC 253; this IMF is similar to a modified Salpeter IMF. The models indicate that rapid massive star formation has been ongoing for 20-30 million years in NGC 253—that is, it is in a late phase of

¹Visiting Astronomer at the Infrared Telescope Facility, which is operated by the University of Hawaii under contract to the National Aeronautics and Space Administration.

²Current address: Tivoli Systems, Stonelake 6, 11000 Mopac Expressway, Suite 400, Austin, TX 78759

its starburst. Its optical spectrum has characteristics of a transitional HII/weak-[O I] LINER. We model the emission line spectrum expected from a late phase starburst and demonstrate that it reproduces these characteristics.

Subject headings: Galaxies: Individual (NGC 253) — Galaxies: Starburst — Infrared: Galaxies

1. Introduction

A significant fraction of nearby galaxies have strong, centrally concentrated infrared sources indicative of rapid star formation in their central few hundred parsecs (Rieke and Lebofsky 1979; Devereux, Becklin, & Scoville 1987). These so-called starburst galaxies make a dramatic contribution to the star formation activity in the local universe; Heckman (1997) calculates that just four galaxies (of which NGC 253 is one) are responsible for 25% of the high-mass star formation within 10 Mpc. Local starburst galaxies serve as a model for galaxy formation and evolution at higher redshifts. An understanding of how these events occur and evolve will require study over the full range of scale and age. At the same time, very detailed modeling is required of the nearest starbursts such as NGC 253 to provide templates for models of less accessible systems.

NGC 253 has been observed extensively in all accessible spectral regions (e.g., radio: Ulvestad & Antonucci 1997; molecular line emission: Mauersberger et al. 1996; far infrared: Carral et al. 1994; mid-IR: Keto et al. 1994, Telesco, Dressel, & Wolstencroft 1993; near-IR: Sams et al. 1994; optical: Watson et al. 1996; X-ray: Ptak et al. 1997; and gamma ray: Paglione et al. 1996). Additional references are given in those cited above. NGC 253 was one of the first galaxies to be studied with an evolutionary starburst model (Rieke et al. 1980). The subsequent observations taken together have substantially expanded on our knowledge of the starburst phenomenon from the inputs to that model, demonstrating the presence of supernovae remnants and HII regions, young ultracompact star clusters, a hot superwind, and a host of other starburst phenomena.

Young starbursts, including NGC 253, are characterized by high levels of interstellar extinction that can make properties deduced from optical measurements unrepresentative (e.g., Rieke et al. 1980; Puxley 1991). Consequently, infrared measurements play a critical role in defining nebular properties, morphologies, rotation curves, and other parameters. We have added to the extensive infrared observations of this galaxy with the deep NIR images covering a wide ($\sim 7'$) field, narrowband images in Br γ and H $_2$, near- and mid-infrared spectra, and a high-resolution spectral map of [Ne II].

Since the first models of M 82 and NGC 253 (Rieke et al. 1980), evolutionary synthesis modeling has become an important component of starburst study (e.g., Doyon, Joseph, & Wright 1994; Leitherer & Heckman 1995 and references therein; Schinnerer et al. 1997). We interpret the new infrared measurements with the other properties of NGC 253 through a modern synthesis

model (Rieke et al. 1993, hereafter RLRT93). In this way, the behavior of NGC 253 can be related consistently to that of other galaxies we have modelled as part of a comprehensive study of nearby starbursts: NGC 6946 (Engelbracht et al. 1996, hereafter ERRL96) and M 82 (McLeod et al. (1993); RLRT93); a number of blue dwarf galaxies (Vanzi & Rieke 1997), and a sample of interacting galaxies (Vanzi et al. 1998). We demonstrate that the NGC 253 starburst is at a relatively late stage of development, during which the high rate of supernova explosions leads to behavior that places it as a transition object between pure starbursts and weak-[O I] LINERs.

This paper is organized as follows: In §2 we describe the observations and the processing we performed on the data. We then use our data and results from the literature to derive physical properties of the starburst in §3. In §4 we use the properties derived in the previous section to constrain evolutionary synthesis models of the starburst. We use the models to explore burst parameters such as age, intensity, IMF, and star formation history. §5 discusses other results obtained from our data or implied by the starburst modeling results. In §6 we summarize the paper.

2. Observations and Data Reduction

2.1. Images

Broadband images in the J, H, and K_s bands as well as narrowband images with 0.5% bandwidth filters tuned to $\text{Br}\gamma$ and the (1,0)S(1) line of H_2 were obtained at the Steward Observatory 1.55m telescope using a camera equipped with a NICMOS3 array. The data were reduced as described in ERRL96. The deep broadband images were flux-calibrated using the UKIRT faint standard number 2 (Courteau 1994). We calibrated the K_s -band image to K-band magnitudes using the standard-star photometry, and will hereafter refer to this image as the K-band image. We have ignored the small color correction between the K_s and K band, since this correction is smaller than the photometric uncertainty.

We present photometry of the nucleus in Table 1 in several circular apertures, plus a region the size of our extracted slit aperture (used to calibrate our spectra.) Photometric errors were estimated from the dispersion in multiple measurements of the standard star at different airmasses and are typically 2% in the J and H bands and 4%-5% in the K band.

The broadband images are presented in Figure 1. The images have a scale of $0''.9$ per pixel and the coordinate system is plotted assuming that the intensity peak of the infrared images corresponds to the position of NGC 253 quoted in NED (Nasa Extragalactic Database): $\alpha(1950) = 00^{\text{h}} 45^{\text{m}} 05^{\text{s}}.9$, $\delta(1950) = -25^{\circ} 33' 40''$. This position closely matches the position of the K-band peak found by Sams et al. (1994).

The narrow-band images are presented in Figure 2. These images are the differences between the on-line and off-line images. In the same figure, we present $J - H$ and $H - K$ color maps of the

nuclear region, which show that the galaxy colors become very red on the nucleus due to strong extinction.

2.2. Near-IR spectra

We obtained long-slit spectra of NGC 253 in the J, H, and K bands at a resolution of ~ 3000 with the Steward Observatory 2.3m telescope using FSpec, a near-infrared long-slit spectrometer (Williams et al. 1993). The slit was centered on the infrared peak of the galaxy with a slit-viewing infrared guide camera. Observing and data-reduction techniques are as described in ERRL96, with the exception that a more precise wavelength calibration was obtained using a set of numerically computed wavelengths for the OH airglow lines (C. Kulesa, private communication).

To correct the spectra for atmospheric absorptions, a spectrum of HR 173, a G3V star about 2° away from NGC 253, was taken close in time to the galaxy observations and was divided into the galaxy spectrum. This step introduced spurious emission features into the spectrum due to intrinsic absorptions in the standard star. To correct for these features, we multiplied our galaxy spectrum by the high-resolution solar spectrum (smoothed to our instrumental resolution) obtained by Livingston & Wallace (1992).

Most of the spectra were obtained with the slit oriented along the major axis of the galaxy, while two key grating settings which cover the (1,0)S(1) line of H_2 , $Br\gamma$, and the (2,0) and (3,1) CO bands were obtained with the slit oriented along the minor axis. The J, H, and K-band spectra are presented in Figures 3, 4, and 5, respectively. Each spectrum is the sum of 10 $1''.2$ pixels along the slit, centered on the intensity peak. We have computed a $1-\sigma$ uncertainty for each point in the spectrum from the dispersion in the set of individual observations. This error spectrum is plotted above each flux spectrum. The flux scale for each spectrum was taken from the broadband images, using the $2''.4 \times 12''$ aperture in Table 1.

We obtained additional spectra of NGC 253 in the J and K bands at a resolution of ~ 1200 using the same instrument and telescope. The slit was again oriented along the major axis of the galaxy and we extracted a similar aperture from these spectra. The spectra were reduced in a similar fashion to the high-resolution spectra, with the exception that our standard star was HR 232, an A3V, so the only correction for intrinsic absorption was to interpolate over the H lines. The use of a hotter standard star (in which metal lines are presumably weak or undetectable at this resolution) to correct these spectra allows us to confirm that our correction for the intrinsic absorptions (other than H) in the standard star used for the high-resolution data was accurate.

The low-resolution spectra (Figures 6 and 7), while lacking some of the detail in the high-resolution ones, give access to several additional [Fe II] and H_2 lines as well as some unidentified features in the J band. The strong features beyond $2.4\mu\text{m}$ not marked as H_2 lines are narrow telluric absorptions which are poorly sampled at our low resolution and which appear as emission features after the spectrum is divided by the standard star. All measurements taken

from the near-infrared spectra are derived from the high-resolution spectra when possible.

2.3. Faint emission lines

A difficulty with interpreting near-infrared spectra of starburst galaxies is that weak nebular emission lines are lost in the structure of the stellar absorption features. To counteract this problem, we have used a library of stellar spectra (to be published separately) to model the galaxy continuum. We selected a suite of fifteen stars which minimized the residual continuum when subtracted from the galaxy spectrum. The resulting mix of stars is thus not optimized in a population synthesis sense, but was empirically chosen to be a good match to the galaxy continuum. We redshifted the stellar spectra to the galaxy velocity, broadened them to match the velocity dispersion in the galaxy (see §3.5.2), scaled them, and subtracted them from the galaxy spectrum. The continuum-subtracted spectra of NGC 253 are shown in the lower parts of Figures 4 and 5. The H-band and K-band flux measurements of emission lines presented in this paper are taken from the continuum-subtracted spectra.

2.4. Mid-IR Spectra

We obtained spectra of the [S IV] 10.5 μm line in NGC 253 using the Irshell spectrograph (Lacy et al. 1989) on the NASA Infrared Telescope Facility. The 10'' long by 2'' wide slit was positioned across the nucleus of the galaxy at PA=61°. Additional spectra were measured with parallel slit positions, one slit width to either side of the nucleus. The 10×64 Si:As array provided 1'' sampling along the slit and a spectral resolution of 30 km s⁻¹. The seeing was poor and the sky was partly cloudy. DC sky levels were monitored to identify frames that were contaminated by clouds. A dome-temperature card, chopped against the sky, was used for flat-fielding, atmospheric correction, and fluxing (Lacy et al. 1989). The data were reduced using a software package developed by Achtermann (1994).

We mapped the [Ne II] 12.8 μm emission from NGC 253 by using Irshell in scanning mode (Lacy & Achtermann 1994), sweeping the slit back and forth across the galaxy by 22''. The off-source positions at the ends of the scans were averaged to produce a sky frame. The data were combined to form a 22''×22'' by 64 spectral channel data cube. A position-velocity plot of the [Ne II] line is shown in Figure 8. The [Ne II] has a spatial extent of 6'' and a velocity width of 150 km s⁻¹ FWHM. The integrated [Ne II] flux is $4.6 \pm 0.1 \times 10^{-11}$ erg s⁻¹ cm⁻². For comparison, Roche & Aitken (1985) report a measurement of 3.3×10^{-11} erg s⁻¹ cm⁻².

The [S IV] spectra showed a compact (2''×2'') continuum source with only a hint of line emission at a level of 5.5×10^{-14} erg s⁻¹ cm⁻². Since the [Ne II] is spread over 6 spatial and 10 spectral pixels, we determined an upper limit of 3.0×10^{-13} erg s⁻¹ cm⁻² on the [S IV] flux by summing over 6 spatial rows (see Figure 9) and 10 spectral pixels.

3. Starburst Parameters

The values of the parameters that characterize the NGC 253 starburst are summarized in Table 2. They have been determined assuming a distance of 2.5 Mpc (de Vaucouleurs 1978), at the low end of the range of 2.5-3.5 Mpc in the literature. As discussed in ERRL96, a small distance places the most conservative constraints on our starburst models.

The reference aperture we will use is $7''$ in radius. We chose this radius because most of the [Ne II], Br γ , and H $_2$ flux (as measured in our spectra and narrow-band images) and the radio flux (as measured in the continuum observations of Antonucci & Ulvestad (1988) or Turner & Ho (1983)) arise from within it. The 10, 20 and 30 μ m maps of NGC 253 from Telesco, Dressel, & Wolstencroft (1993) as well as the far-infrared measurements by Smith & Harvey (1996) also show that most of the mid- and far-infrared flux is produced in this region.

3.1. Extinction

We can use line ratios from our spectra to determine the extinction. If the hydrogen recombination line ratios from Table 3 obey Case B, a foreground screen model with $A_V = 9.2 \pm 0.7$ can fit them (c.f. Calzetti, Kinney, & Storchi-Bergmann 1996). (We have used an analytical fit to the Rieke & Lebofsky 1985 extinction law, the Hummer & Storey 1987 theoretical recombination line ratios, and have included an 8% uncertainty in the relative flux calibration in the line ratio uncertainties.) This fit roughly agrees with the Br α strength (Beck & Beckwith 1984). However, the mm-wave H recombination lines still suggest that a significant amount of ionized gas may be hidden by extreme optical depths (Puxley et al. 1997). The ratio of [Fe II](1.257 μ m) to [Fe II](1.644 μ m) should be 1.35 according to the A-values of Nussbaumer & Storey (1988), although this value is subject to some uncertainty. The observed value is 0.68 ± 0.07 (Table 4), which implies $A_V = 8.42 \pm 1.26$, consistent with the estimate from the H recombination lines.

The colors of our broadband images can also be used to estimate extinction. A typical evolved stellar population has $J - H$ and $H - K$ colors of 0.7 and 0.2 (Aaronson 1977), and our starburst models (RLRT93) show that the same is true for the starburst population. Our spectra show that the near-infrared continuum is dominated by starlight, as the strengths of the absorption features are typical of a population of supergiants and are consistent between the H and K bands, thus arguing against veiling by a featureless continuum. Therefore, we can assume that colors redder than nominal are purely due to reddening.

From Table 1, the near-infrared colors in our $15''$ reference aperture are $J - H = 1.09$ and $H - K = 0.66$, implying color excesses of 0.39 and 0.46, respectively. Using an analytical fit to the Rieke & Lebofsky (1985) extinction law and a foreground screen geometry for the dust, $E(J - H) = 0.39$ corresponds to 4.26 ± 0.91 magnitudes of visual extinction while $E(H - K) = 0.46$ implies $A_V = 7.35 \pm 1.33$. The extinction values in the near-infrared bands implied by our $H - K$

color are $A_J = 2.00 \pm 0.36$, $A_H = 1.33 \pm 0.24$, and $A_K = 0.87 \pm 0.16$. The extinction to the stars appears to be slightly smaller (at $\sim 3\sigma$ significance) than that to the ionized region.

If we adopt a more realistic dust geometry than a foreground screen, such as the "starburst" model of Witt, Thronson, & Capuano (1992), we obtain a better fit to the observed colors. The colors in the nuclear region of NGC 253 are slightly redder than the most heavily extinguished models presented by Witt et al., so we have used polynomial fits to extrapolate beyond their values. The models imply a total extinction to the center of the system, $A_V(\text{cen})$, of 17.27 ± 6.78 and 19.07 ± 3.32 , based on the $J - H$ and $H - K$ excesses respectively. Although this model contains much more total dust than a foreground screen model, much of the light comes from relatively unextinguished stars, so that the implied average equivalent extinction is similar to the foreground screen case. The equivalent extinction values in the near-infrared are $A_J = 1.64 \pm 0.51$, $A_H = 1.24 \pm 0.43$, and $A_K = 0.85 \pm 0.30$ from the $J - H$ color and $A_J = 1.84 \pm 0.32$, $A_H = 1.40 \pm 0.24$, and $A_K = 0.94 \pm 0.16$ from the $H - K$ color.

Since the equivalent extinction values in the near infrared are similar for the two dust geometries, the near infrared fluxes can be corrected reliably. We will adopt extinction values that are an average of those derived from the mixed model: $A_K = 0.90 \pm 0.17$, $A_H = 1.32 \pm 0.25$, and $A_J = 1.74 \pm 0.30$.

We have used the $H - K$ color map to deredden our K-band image. We assumed that the intrinsic $H - K$ color of the galaxy was 0.2 (so that $E(H - K) = (H - K) - 0.2$) and converted the color excess to a dereddening map using the Rieke & Lebofsky (1985) extinction law. The K-band image was then multiplied by the dereddening image to produce the extinction-corrected K-band image of the galaxy presented in Figure 10. We also deprojected the dereddened image by stretching it along the minor axis by a factor $1/\cos(i)$, where we have taken $i = 78^\circ$ (Pence 1981). The resulting image is also presented in Figure 10.

3.2. [Fe II] emission

The high sensitivity and broad wavelength coverage of our near-infrared spectra has allowed us to measure seven [Fe II] lines, listed in Table 4, allowing an estimate of the electron density in the [Fe II]-emitting region. We use the ratios $\lambda 1.279\mu\text{m}/\lambda 1.644\mu\text{m}$ and $\lambda 1.533\mu\text{m}/\lambda 1.644\mu\text{m}$ and the models of Bautista & Pradhan (1996). In the range of interest, the diagnostic ratios we have chosen are essentially independent of temperature. We have plotted the values of these two line ratios (corrected for extinction) as a function of density in Figure 11. For each curve, we have marked the range consistent with the observations as a shaded box, indicating a mean density of $\sim 5000 \text{ cm}^{-3}$.

[Fe II] emission in starbursts is thought to arise predominantly from supernova remnants. For example, Greenhouse et al. (1991) find peaks on bright radio compact sources in the [Fe II] surface brightness in M 82. However, these compact sources account for only a small fraction of the

total [Fe II] emission. Forbes & Ward (1993) find a correlation between nonthermal 6cm emission and [Fe II]. However, the trend line is offset from that for supernova remnants. Vanzi & Rieke (1997) explain this offset in terms of the short lifetime for the [Fe II]-emitting stage in a supernova remnant. Our data add to the arguments favoring a supernova origin for the [Fe II], since the density we derive is in good agreement with that observed in the supernova remnants observed by Oliva, Moorwood, & Danziger (1989).

Vanzi & Rieke (1997) used the observed supernova rate in M 82 to derive a relation between the [Fe II] luminosity and the supernova rate. To apply this relation, we correct our observed [Fe II] ($\lambda 1.644\mu\text{m}$) flux (from Table 4) to a $15''$ aperture using the ratio of the K-band fluxes in the $15''$ and $2.4 \times 12''$ apertures (this scaling is reasonable because the K-band flux is dominated by cool supergiants which are the immediate precursors to the supernova remnants). We also correct for 1.33 magnitudes of extinction. We obtain a total [Fe II] flux of $3.8 \times 10^{-12} \text{ erg s}^{-1} \text{ cm}^{-2}$, or a luminosity of $2.8 \times 10^{39} \text{ erg/s}$. The Vanzi & Rieke relation then implies a supernova rate of 0.03 per year. If the [Fe II]-emitting phase of each supernova remnant lasts $\sim 10^4$ years, this rate implies that there are currently ~ 300 [Fe II]-emitting supernova remnants in the nucleus of NGC 253.

Ulvestad & Antonucci (1997) find an upper limit on the supernova rate of 0.3 yr^{-1} . The supernovae have also been modeled by Colina & Pérez-Olea (1992), who estimate a rate of 0.05 yr^{-1} , and by Van Buren & Greenhouse (1994) and Paglione et al. (1996), who both find 0.08 yr^{-1} . These estimates are all based on modeling supernova counts and hence are to first order distance-independent. The SN rate can also be estimated from other luminosities than that of [Fe II]. For example, if we assume the nonthermal radio flux from Turner & Ho (1983) is entirely due to synchrotron emission from supernova remnants, we can derive a supernova rate of 0.03 yr^{-1} using equation (8) of Condon & Yin (1990).

All of the other rate estimates are in satisfactory agreement with our estimate using the [Fe II] emission. Both of the luminosity-based estimates are lower than those from supernova counts by a factor of about two. Although this difference is probably within the errors, if the galaxy were at 3.5 Mpc (within the uncertainty in distance), the luminosity-based rates would double and the agreement would be improved.

3.3. Temperature of the Hot Stars

The difference in ionization potentials of S^{++} and Ne^0 makes the [S IV]/[Ne II] ratio a sensitive indicator of the effective temperature of the UV radiation field. The ratio is also dependent on the relative abundances of sulphur and neon, but the strong temperature dependence should dominate in our data. We apply an extinction correction of $A_V = 14 \text{ mag}$ to the mid-infrared data, based on the $\text{Br}\alpha/\text{Br}\gamma$ data of Rieke et al. (1980). This large extinction only changes the [S IV]/[Ne II] color by 0.26 dex (Rieke & Lebofsky 1985) to $\log([\text{S IV}]/[\text{Ne II}]) = -2.7$, or a 3σ upper limit of

–1.9. We compare these values to single star photoionization Cloudy (Ferland 1993) models to determine effective temperatures as a function of ionization parameter, obtaining upper limits of 36000 K, 38000 K, and 49000 K respectively for $\log U = -1.5$, -2.5 , and -3.5 . The weak detection of [S IV] on the central slit position implies effective temperatures of 34400 K, 36000 K, and 42300 K for the respective $\log U$ values.

The main problem with this technique is the strong dependence of the [S IV]/[Ne II] ratio on ionization parameter. The Lyman continuum flux is 10^{53} s^{-1} (see §3.6). From Figure 2, we see that all of the Br γ flux comes from within a radius of $7''$, or 90 pc. From Heckman et al. (1990), the nucleus has an electron density of at least 600 cm^{-3} and probably higher since dust would have hidden the nucleus at 6700 \AA . An electron density range of $600\text{-}1000 \text{ cm}^{-3}$ gives $-\log U = 2.2 - 2.5$. It would take a large amount of substructure in the nucleus with a density of $n_e = 10^4 \text{ cm}^{-3}$ to give $\log U = -3.5$.

For the $\log U = -1.5$ and $\log U = -2.5$ cases, we examined a two star model, one star with $T = T_{eff}$ and the other with $T = 40000 \text{ K}$. We determined how bright the 40000 K star would have to be relative to the T_{eff} star to alter the [S IV]/[Ne II] ratio by 0.15 dex, or roughly 1σ . For the four cases: $\log U, T_{eff} = -1.5, 34400$; $-1.5, 36000$; $-2.5, 36000$; $-2.5, 38000$ we found that the 40000 K star contributed the following percentages of the Lyman continuum photons: 2.5; 7.4; 6.8; 31. These percentages can be combined with the starburst models of Section 4 to determine the age of the starburst. As discussed below, the effective temperature is unlikely to be as high as 38000 K, so a conservative upper limit to the ionizing flux contribution by stars hotter than 40000 K is probably 15%.

Vanzi et al. (1996) suggested that the ratio HeI(1.7)/Br10 is useful to constrain the temperature of the hot stars because it is not heavily affected by reddening or electron temperature. Our upper limit for the $1.7\mu\text{m}$ HeI line (Table 5) corresponds to an upper limit of $\text{HeI}(1.7)/\text{Br}10 \leq 0.2$, placing an upper limit of $\sim 37,000\text{K}$ on the stellar temperature exciting the ISM. Carral et al. (1994) use the far infrared fine structure lines to derive an effective temperature for the exciting stars of $34,500 \pm 1,000\text{K}$.

Thus, three independent means of estimating the temperature of the exciting stars from infrared spectra give consistent results of $T_{eff} < 37,000 \text{ K}$. The [O III]/H β ratio would give a value a few thousand degrees higher than the infrared indicators. However, we show in Section 5.4 that a significant portion of the [O III] may be shock-excited in supernova remnants. Also, at ~ 0.4 solar and higher metallicities, it is expected that [O III]/H β and other optical indicators will overestimate the temperature of the photoionizing field for a variety of reasons, such as an increase in electron temperature due to depletion onto grains or to photoelectric heating (Shields & Kennicutt 1995). Our CLOUDY models show the infrared-line-derived temperatures to be virtually independent of electron temperature (c.f. Vanzi et al. 1996).

3.4. Luminosity

In a dusty region full of young stars (such as a nuclear starburst) much of the stellar radiation is reprocessed by dust, so the far-infrared luminosity serves as a reliable estimate of the integrated output of the hot stellar population. We have estimated a luminosity of $1.1 \times 10^{10} L_{\odot}$ from measurements at 1.3mm (Krügel et al. 1990), the submillimeter (Gear et al. 1986), the far-infrared (Smith & Harvey 1996, plus IRAS measurements from Rice et al. 1988), and the mid-infrared (Rieke & Low 1975). The small-beam measurements by Smith & Harvey proved useful in determining the fraction of luminosity actually arising from the starburst, as the scans of Rice et al. show that a non-negligible fraction of the far-infrared luminosity in NGC 253 is due to a cool extended component. This value should be considered a lower limit to the total luminosity, since a significant amount of energy may be escaping perpendicular to the plane of the galaxy.

We have computed a lower limit to the K-band luminosity of the underlying stellar component by fitting an exponential disk model to the K-band light at large radii (c.f. Forbes & Depoy 1992) and computing the integrated light contribution of this model in the central $15''$. The absolute K magnitude of this component is -18.3 , less than 15% of the total K-band light after accounting for extinction. Virtually any more sophisticated model, such as allowing the old stars to be more centrally concentrated, will increase this proportion.

Using $BC_K = 2.7$ and $M_{\text{Bol}}(\odot) = 4.75$, we compute that the bolometric luminosity of the underlying population is less than $2 \times 10^8 L_{\odot}$, or less than 2% of the observed value, so we will ignore this small contribution to the total. However, we have subtracted the K flux from the older stars from the total to derive the expected starburst output at this wavelength, and it is this corrected value which appears in Table 2.

3.5. Mass

3.5.1. Rotation

An abundance of kinematic data exists for the nuclear region of NGC 253. Several rotation curves exist in the literature that have been obtained at radio wavelengths, in molecular emission lines such as CO (e.g., Mauersberger et al. 1996, Canzian et al. 1988) or CS (Peng et al. 1996) or in hydrogen recombination lines (Anantharamaiah & Goss 1996). While most of these observations have high spectral resolution, they typically have poor spatial resolution and are not always useful for probing the dynamics very close to the nucleus. The data of Anantharamaiah & Goss are an exception — their data have a spatial scale similar to ours and indicate a mass of $3 \times 10^8 M_{\odot}$ inside a radius of $5''$, comparable to the mass we derive in the next section.

Optical rotation curves of the nuclear region also exist (e.g., Muñoz-Tuñon, Vilchez, & Castañeda 1993 and Arnaboldi et al. 1995). The observations by Muñoz-Tuñon et al. are likely affected by dust extinction in the sense that they indicate a rotation curve that is too shallow

(as demonstrated by Prada et al. 1996). The measurements by Arnaboldi et al. were obtained at higher spatial resolution and indicate a slope for the rotation curve that is somewhat higher than indicated by our data (see below).

In Figure 12 we present rotation curves in strong emission lines and in the (2,0) rovibrational band of CO at $2.3\mu\text{m}$. The stellar CO feature has the advantage that it traces a component of the galaxy nucleus which is not affected by non-gravitational processes such as shocks or winds. The stellar feature also traces a component of the population which is smoothly distributed throughout the region of interest, as indicated by our K-band image. Tracers such as $\text{Br}\gamma$ and H_2 are likely concentrated in discrete HII regions and the surfaces of molecular clouds, although the rotation curves derived from both the gaseous and stellar features match quite well in the central region.

The velocity gradients across the nucleus along the major axis are tabulated for our three chosen near-infrared features in Table 6. They overlap within the uncertainties, and the combined average is $7.5 \pm 0.3 \text{ km s}^{-1}/''$. This number is not corrected for inclination. Our infrared emission lines probably trace a compact nuclear disk of gas. Although there is no way to be certain that the inclination of the nuclear region follows that of the rest of the galaxy, the only correction we can reasonably make is to correct for this inclination, which is 78° (Pence 1981). This correction gives us a value of $7.7 \pm 0.3 \text{ km s}^{-1}/''$. This value is similar to that from Puxley & Brand (1995) but somewhat lower than we find from the data of Prada et al. (1996), from which we calculate 7.8 ± 0.4 and 9.8 ± 0.2 , respectively, if we eliminate points that are obviously not on a linearly-rising rotation curve. The rotation curve indicated by all the near-infrared measurements is quite shallow, however, and indicates a mass of $1.7 \times 10^8 M_\odot$ within a $10''$ radius (the radius at which the rotation curve turns over) if we assume the mass is distributed spherically.

We have also obtained a rotation curve for the well-studied galaxy NGC 3115 as an evaluation of our techniques to measure galaxy rotation. In Figure 12, we compare our results with the optical data of Kormendy & Richstone (1992). The rotation curves compare quite well, although the Kormendy & Richstone rotation curve rises more steeply in the center, most likely due to better seeing and their smaller pixel size ($0''.435$) as compared with our $1''.8$ pixels at the 1.55m telescope. This comparison gives us confidence that we are correctly measuring the galaxy dynamics, despite the fact that the CO band is a broad and one-sided feature.

3.5.2. Dispersion

A more robust way to determine the mass is to measure the velocity dispersion of the stars and compute the mass by assuming a model for the stellar distribution, as in Shier et al. (1994). Using the cross-correlation routines described by Shier et al. , we measure a stellar velocity dispersion in the CO(2,0) feature of $87 \pm 10 \text{ km s}^{-1}$ in the $12''$ aperture we used to extract the spectra, where the error bars include both the statistical uncertainty as measured by a Monte Carlo simulation and an estimate of the systematic uncertainty as determined by experiments

with fitting standard stars. The template star for this calculation was HR 7475.

The observed velocity dispersion is the sum of the dispersions in each extracted pixel, weighted by the luminosity profile of the galaxy. We fit a profile to the $2.3\mu\text{m}$ region of our spectrum of NGC 253, modeling the light distribution using the η models of Tremaine et al. (1994). The model that best fit the luminosity profile has a scale radius of $6''$ (about 73 pc at the distance of NGC 253) and $\eta = 3$. Using this galaxy profile, we measure a mass of $3.9 \pm 0.9 \times 10^8 M_\odot$ within a $7''.5$ radius. The uncertainties in the mass determination are dominated by uncertainties in the velocity dispersion, as the derived mass depends on the square of the velocity.

3.5.3. Mass Budget

To determine the mass we may allocate to star formation in a recent starburst, we must subtract from the dynamical mass the mass of the old stars and molecular gas in the nucleus. Assuming the same conversion from mass to K-band luminosity determined by ERRL96 and the K-band luminosity derived in §3.4, this preexisting stellar population is expected to have a mass of at least $3.3 \times 10^8 M_\odot$, and is likely to be large enough that it accounts for virtually all the stellar mass in the nucleus. The large proportion of mass in old stars confirms the theoretical predictions that a starburst will be triggered when only 10-20% of the nuclear mass is in the form of gas (Wada & Habe 1992; Bekki 1995). Using the standard CO to gas mass conversion, the molecular gas mass may be as large as $1.4 \times 10^8 M_\odot$ (Mauersberger et al. 1996). Uncertainties in the application of this conversion to starburst galaxies (e.g., Maloney & Black 1988; Shier et al. 1994) led Mauersberger et al. to propose a much smaller mass of $\sim 3 \times 10^7 M_\odot$ based on measurements of dust continuum and a rare isotope of CO.

The lower limit on the mass in old stars and the gas combined leave no more than $0.3 \pm 0.9 \times 10^8 M_\odot$, or a strong upper limit of $2.1 \times 10^8 M_\odot$ on the starburst mass; it is likely much less. We show in §4 that the best-fitting starburst models indicate a mass of a few times $10^7 M_\odot$.

3.6. Ionizing Flux

To estimate $Q(\text{H})$ (number of hydrogen ionizations per second), we correct the longest-wavelength (i.e., the line least affected by extinction) hydrogen recombination line flux we observe ($\text{Br}\gamma$) for extinction and convert it to $Q(\text{H})$ using the ratio $I(\text{H}\beta)/I(\text{Br}\gamma) = 30.3$ (from Hummer & Storey 1987) and $\alpha_{\text{B}}/\alpha_{\text{H}\beta}^{\text{eff}} = 8.40$. From our narrow-band images, we determine the $\text{Br}\gamma$ flux in a $15''$ aperture to be $9.16 \times 10^{-13} \text{ erg s}^{-1} \text{ cm}^{-2}$. We correct this flux to $2.14 \times 10^{-12} \text{ erg s}^{-1} \text{ cm}^{-2}$ using $A_K = 0.9$ from §3.1. The value of $Q(\text{H})$ implied by this $\text{Br}\gamma$ flux is $1.0 \times 10^{53} \text{ s}^{-1}$.

We obtain a similar value from our $[\text{Ne II}]$ measurement. The dereddened ($A_V=14 \text{ mag}$) $[\text{Ne II}]$ flux is $(6.6 \pm 0.2) \times 10^{-11} \text{ erg s}^{-1} \text{ cm}^{-2}$. Combined with the formula of Roche et al. (1991)

and a distance of 2.5 Mpc, this gives $N_{\text{LyC}} = 1.3 \times 10^{53}$ photons s^{-1} . The Roche et al. formula assumes a solar abundance of neon. While the actual neon abundance in NGC 253 is unknown, the fact that this number is within 30% of the value derived from the $\text{Br}\gamma$ flux suggests that the neon abundance is not too different from solar.

We obtain a very similar $Q(\text{H})$ from the thermal radio flux measured by Turner & Ho (1983), using their equation for converting the thermal component of the 6cm radio flux to $Q(\text{H})$. They estimate that 125mJy, or less than 10% of the total flux at 6cm, is due to thermal emission, implying $Q(\text{H}) \sim 8 \times 10^{52} \text{ s}^{-1}$. A somewhat higher estimate, $Q(\text{H}) = 3.7 \pm 0.8 \times 10^{53} \text{ s}^{-1}$, is derived by Puxley et al. (1997) from mm-wave H recombination lines.

These numbers would be approximately equal to the total number of ionizing photons per second, N_{LyC} , were it not for the presence of significant amounts of dust in the starburst region which can compete with hydrogen atoms in absorbing ionizing photons. As such, we can take $Q(\text{H})$ to be a lower limit on N_{LyC} , i.e., $\log(N_{\text{LyC}}) \gtrsim 53$.

3.7. CO index

We have listed the equivalent widths of the CO lines, along with other absorption features, in Table 7. Using the definition of the CO index by Kleinmann & Hall (1986), where we have redshifted the wavelengths by 245 km s^{-1} , our spectroscopic CO index is 0.31, which corresponds to a photometric index of 0.18. If we deredden the spectra using the extinction described in §3.1, our spectroscopic index is 0.32, for a photometric index of 0.19. Using the specification of Doyon, Joseph, & Wright (1994a), we measure $CO_{sp} = 0.29$, which gives $CO_{ph} = 0.21$.

Although both approaches agree well, the Doyon et al. approach is more appropriate for data of lower resolution than ours: we will therefore use the Kleinmann and Hall definition. We will correct our measured value for dilution by an underlying population by assuming that the old stellar population contributes $\sim 15\%$ of the K-band light (see §3.4) and that the old population has a CO index of 0.15 (Frogel et al. 1978), giving us an intrinsic CO index of 0.20 for the starburst population.

3.8. Other Constraints

Fabbiano (1986) shows that NGC 253 has a large X-ray feature out of the plane of the galaxy and extending at least to 7 kpc. She suggests that this source is due to hot gas escaping from the galaxy in a starburst-driven superwind. A similar feature in M 82 was used in RLRT93 to place timing constraints on the starburst in that galaxy, based on the interval from the initiation of supernova explosions to when the hot gas could expand to create the feature. Similar constraints should hold for NGC 253. For example, in a simple single-burst model, an interval of about 8 Myr

must pass from the peak of the star formation to allow gas to expand out of the starburst region in NGC 253.

As in M 82, it appears that the metallicity in the NGC 253 starburst is approximately solar or less than solar rather than highly enriched (e.g., Carral et al. 1994; Ptak et al. 1997). The oxygen abundance is of particular interest because this element is released copiously in supernovae (Arnett 1978). Although RLRT93 speculated that highly ionized oxygen might hide in the hot superwind, recent X-ray spectra indicate that, if anything, the abundance is less than solar in this plasma (Ptak et al. 1997). Although there is some controversy about the low metallicities derived from X-ray data (Fabbiano 1996), any model for the starburst that produces high oxygen abundances is likely to be inconsistent with observation.

4. Starburst models

4.1. Description of Models

RLRT93 fitted the starburst in M 82 using the models of Rieke et al. (1980) with updated stellar tracks and atmospheric parameters. The starburst model uses the grid of stellar evolution tracks of Maeder (1992), which have been assigned observational parameters based on a combination of atmosphere models and empirical calibration. The models include stars up to $80M_{\odot}$ and interpolate between the tracks to reduce oscillations caused by discreteness in the stellar masses. Further details can be found in RLRT93.

4.2. NGC 253 models

For NGC 253, the model values of N_{LYC} , L_{Bol} , CO index, K-band flux and ν_{SN} (supernova rate) are displayed as a function of time in Figure 13. Each point along the curves has been divided by the observed values for NGC 253 in Table 2, so the target value for each quantity is 1. A fit can be considered good when all curves meet the target value simultaneously. In practice, since some of the observational parameters are uncertain or are merely lower limits, we choose the point on the plot where the curves can simultaneously meet the target values within the specified range of uncertainty.

The various input parameters constrain the starburst model in different ways, depending on how each is determined. Our value for N_{LYC} must be considered a lower limit. Given the uncertainties due to poor angular resolution in the far infrared and to energy escaping perpendicular to the plane of the galaxy, we require our models to match the observed L_{Bol} to within 50%. The formal uncertainties in our determination of the CO index and K-band flux are small, but due to uncertainties about continuum placement and corrections for extinction, we assign uncertainties to these quantities of 20%. The supernova rate is probably no more certain

than a factor of two; however, since our estimate is generally on the low side compared with those derived by other means, and this discrepancy cannot be removed in the starburst models by changing the distance to the galaxy (since the supernova rate and other luminosity-derived parameters will scale together), we prefer models that do not fall significantly below the estimated rate. We have also made use of the temperature constraint derived in §3.3. In the figure, we plot a curve labeled $T(\text{UV})_{40}$, which is the ratio of the total ionizing flux to the ionizing flux produced by stars hotter than 40,000 K. The starburst model is required to age sufficiently that no more than 15% of the ionizing flux comes from stars hotter than 40,000 K.

We created two models with a simple, single-burst model, with the star formation rate a Gaussian in time with a FWHM of 5 million years. The models begin 5 million years before the peak of the star formation. This short Gaussian burst of star formation is very efficient in converting stellar mass to luminous output.

Our first model used a solar-neighborhood IMF (RLRT93’s IMF3). Using a mass of $9 \times 10^7 M_{\odot}$, the model comes closest to the constraints at a time of 5.5 million years after the peak of the star formation. The CO index, the ionizing flux, and K-band luminosity are very close to the observed values, while the bolometric luminosity is a factor of 30% higher than observed and the supernova rate is a factor of 2 too low. There has been inadequate time for supernovae to eject a hot plasma to the observed extent of the X-ray emission. This model falls short of the observational constraints, despite our conservatism in setting them. The model also makes the uncomfortable prediction that the star formation efficiency is 40-75%, assuming the mass not used to make stars is still in the form of molecular gas.

We also attempted to model the starburst using an IMF more biased towards the formation of massive stars. Such a model produces much more luminosity for a given mass and should do a better job of fitting the observations of NGC 253 while remaining within the mass constraint. We used the IMF found by RLRT93 to fit the M 82 observations best (their IMF8). This model looks very similar to the IMF3 one, but it only uses $3.5 \times 10^7 M_{\odot}$.

To illustrate how the uncertainties in the various parameters affect the determination of the mass and age of the starburst, in Figure 14 we have plotted the range of allowed values for each quantity constraining the starburst for the IMF8 model. For example, the two dot-dashed lines in the plot indicate a range of 20% around the nominal K-band luminosity. Quantities such as the CO index and $T(\text{UV})_{40}$ do not scale with mass and so serve primarily as age constraints, showing up as vertical lines on this plot, where the $T(\text{UV})_{40}$ is a lower limit and the CO index has an allowed range which extends off the far end of the plot. The hatched region indicates the space in the (mass, age) plane that can be occupied by the model while still matching the observations. In this case, the primary constraints are the lower limits on the supernova rate and the UV flux and the upper limits on the K-band luminosity and the bolometric luminosity. The model falls a little short of meeting the constraints at $3.5 \times 10^7 M_{\odot}$ —a better fit occurs at 6 million years after the peak of star formation, using a mass of $3.8 \times 10^7 M_{\odot}$. However, the figure illustrates that no

single burst model approaches the X-ray timing constraint (at ~ 13 Myr, 8 Myr after the peak of star formation).

We next explored the effect of varying the star formation history by adding a second burst. We have parameterized this second burst by a time delay (Δt) after the initial burst and a fraction (f) of the mass consumed by both bursts that goes into the second burst, so that $f = 0.5$ implies identical masses for both bursts. Although the additional parameters introduced by a two-burst model can help fit many constraints, they invariably require increased mass (RLRT93). Consequently, since the IMF3 model already used a lot of mass, we have not computed double burst models for it. In Figure 13 we display a model with two IMF8 bursts of equal strength, separated by 25 million years. Since we have diluted the mass available by putting it into two widely-separated bursts, this model requires a total mass of $6 \times 10^7 M_{\odot}$. The model achieves a good fit at a time of 34.5 million years. The two main advantages of this double-burst model are that there is adequate time for expansion of the X-ray superwind and that the supernova rate is in reasonable agreement with the target value. Models with shorter time intervals between bursts predict supernova rates below the target value.

Although for convenience in modeling, we have used two separated bursts in this model, similar results would be obtained with other time dependencies for the star formation rate, so long as: 1.) a substantial portion of stars formed about 30 million years ago, so they can produce supernovae without ionizing flux; and 2.) the star formation rate has decayed rapidly for the last roughly 5 million years, so the correct ionizing flux can be produced without an excess of very hot stars.

4.3. Residual Problems

These three models only meet the temperature constraint with difficulty - if we reduce the allowed fraction of ionizing photons emitted by stars hotter than 40000 K from 15% to 10%, significantly more mass is required. The temperature constraint is satisfied trivially if we arbitrarily impose an upper-mass cutoff on the models. This explanation is unlikely, however, since observations of very young star formation regions always indicate that very massive stars are formed (e.g., Conti, Leitherer, & Vacca 1996; Leitherer et al. 1996). Extending the duration of the burst of star formation, as in the model we present in the last panel, only aggravates the temperature problem, as a larger fraction of the ionizing flux is produced by recently-formed massive stars. It might be thought that the dusty environments of starbursts would absorb hard UV photons and soften the ionizing spectrum. However, the absorption properties of dust are believed to *harden* the UV ionizing spectra (Aannestad 1989; Shields & Kennicutt 1995).

The lack of extreme oxygen over abundance is a strong constraint on the shape of starburst IMFs at the highest masses (RLTRT93). The evidence from X-ray spectra that the oxygen may be underabundant relative to solar in NGC 253 (and M 82) (Ptak et al. 1997) therefore may add a

difficult constraint to the models, unless the amount of oxygen returned to the ISM is lower than expected.

4.4. The “Biased” Initial Mass Function in NGC 253

Although the case is not as definitive as in extreme galaxies like M 82 (RLRT93) and NGC 1614 (Shier, Rieke, & Rieke 1996), NGC 253 appears to be another example of a starburst that cannot be modelled easily with a “local” IMF such as that of Scalo (1986). IMF8 was adopted for M 82 after consideration of a broad range of alternatives, and appears to be a satisfactory solution to this problem for NGC 253 also.

The presence of a starburst IMF biased toward high mass stars continues to be controversial (e.g., Satyapal et al. 1997). However, many studies have fitted starburst observations with a “Salpeter” IMF, with a slope of -1.35 but with a turnover at low masses to satisfy observations of the local stellar population (e.g., Conti, Leitherer, & Vacca 1996; Satyapal et al. 1997). This IMF is virtually identical in observable properties to IMF8 and differs just as strongly from the IMF of Scalo (1986)! For example, if the “Salpeter” IMF adopted by Satyapal et al. (1997) is normalized to IMF8 through the requirement that the stellar populations have equal total mass, the two IMFs are the same in the critical 15-30 M_{\odot} region except for a small difference in slope. The “Salpeter” IMF predicts a larger number of very massive stars than does IMF8, and would exacerbate the problem with oxygen abundance.

There are substantial difficulties in determining the local IMF, and the IMF above $\sim 1 M_{\odot}$ in other environments shows substantial variations either from intrinsic differences or interpretive errors (Scalo 1998). The debate about biased IMFs in starbursts is therefore no longer very relevant. The most interesting development is how all investigators of starburst galaxies have converged on an IMF very similar to IMF8 of RLRT93.

5. Other results

5.1. Continuum morphology

A striking feature of the images in Figure 1 is the bright, elongated feature centered on the nucleus and oriented roughly east-west. This feature was first noted by Scoville et al. (1985), who describe it as a bar; Pompea & Rieke (1990) found that it curves as it approaches the nucleus and suggested it might instead be inner spiral arms. Our deep infrared images indicate that this apparent curvature arises from a zone of strong extinction. Our dereddened K-band image presented in Figure 10 leaves little doubt it is a bar.

Also evident is a ring with a diameter of $\sim 350''$ (~ 4 kpc) along the major axis of the

galaxy. This ring is very nearly circular, as can be seen in our deprojected image of the galaxy in Figure 10. The ring is also apparent in the deep H-band image from Forbes & DePoy (1992), although they do not discuss it. The bar crosses the ring and also has a length of $\sim 350''$.

Canzian, Mundy, & Scoville (1988) show a bar in CO emission that is about $30''$ long and oriented along the stellar bar discussed above. Thus, the configuration of molecular gas in the nucleus of NGC 253 approximates the theoretical predictions that mutual torques between stellar and gas bars will allow the gas to lose angular momentum and sink into the nucleus, where it concentrates until instabilities set in that trigger a starburst.

5.2. Emission-line morphology

In Figure 8 we present position-velocity diagrams of some strong emission lines in NGC 253. These images and the narrow-band images in Figure 2 show that the starburst is not distributed symmetrically along the major axis but instead is concentrated in a region north-east of the nucleus. They also show significant differences from line to line. The H recombination and [Ne II] have a very similar asymmetric distribution in position/velocity space. The [Fe II] is distributed symmetrically to both sides of the nucleus. The H₂ emission is distributed over a broader region still (~ 500 pc). These behaviors are consistent with the starburst originally being fairly uniformly distributed around the nucleus, as indicated by the supernovae traced by [Fe II], but now being active primarily on the nucleus and to the northeast. They also indicate that the H₂ emission is partially excited by a mechanism that extends outside the other starburst indicators, e.g., molecular cloud collisions.

5.3. H₂ emission

The excitation mechanism of H₂ in starburst galaxies is under debate. The strong UV flux should excite a significant amount of H₂. However, many of these galaxies display strong emission in the (1,0)S(1) line (e.g., Goldader et al. 1996) but not in other H₂ lines, suggesting that collisional processes rather than fluorescent ones dominate (c.f., Black & van Dishoeck 1987).

One reason that UV-excited H₂ is so difficult to detect is that its energy is emitted in a huge number of lines, whereas thermally excited H₂ emits most of its luminosity in just a few. In low density gas, fluorescent H₂ emits just 1.6% of its infrared luminosity in the readily observed (1,0)S(1) line while thermally excited H₂ emits 9% of its infrared luminosity in this line. Despite the difficulties associated with detecting a number of very weak lines, fluorescent H₂ has been detected recently in some galaxies (Doyon et al. 1994; Kulesa et al. 1998.)

The combination of high resolution and sensitivity, broad spectral coverage, and our technique for subtracting the stellar continuum allow us to measure an unprecedented number of H₂ lines in

an extragalactic source (Table 8). We have used the A-values, energy levels, and statistical weights adopted by Ramsay et al. (1993) to derive the temperatures listed in Table 9. The temperature derived from the two strongest lines, (1,0)S(1) and (1,0)S(3), is consistent with 2000 K and not with 1000 K. In Table 8, we have also listed a set of line ratios dereddened using the extinction derived in §3.1. We compare these line ratios to two H₂ models from Black & van Dishoeck (1987)—a UV-excited model (their model 14), plus a collisionally-excited model appropriate for 2000 K (their model S2).

A first glance would suggest that the excitation of the H₂ is dominated by collisions, rather than UV pumping. Following the arguments of Kulesa et al. (1998), however, we can show that fluorescent emission plays an important role in producing the H₂ spectrum of NGC 253. In the table we present a mixed model in which 25% of the flux in the (1,0)S(1) line is due to fluorescence, modifying the other line ratios accordingly. One can see that this model fits the data significantly better, without looking radically different from a pure thermal model. The ability to distinguish between pure thermal and mixed thermal and fluorescent H₂ emission depends on having high-enough sensitivity and resolution to detect faint lines.

For a quantitative comparison, we measure a flux in the (1,0)S(1) line of 1.2×10^{-13} erg s⁻¹ cm⁻² in our 2''.4 × 12'' spectroscopic aperture. We correct this value to a 15'' reference aperture using the narrow-band H₂ image and obtain a flux of 3.5×10^{-13} erg s⁻¹ cm⁻². Correcting this value for extinction gives us 8.4×10^{-13} erg s⁻¹ cm⁻², or 1.6×10^5 L_⊙ at a distance of 2.5 Mpc. Using this luminosity, the total H₂ luminosity in the mixed model is 3.8×10^6 L_⊙— 1.3×10^6 L_⊙ from thermal emission and 2.5×10^6 L_⊙ due to fluorescent emission; that is, nearly two thirds of the total H₂ infrared luminosity is derived from fluorescence.

Luhman et al. (1994) report global observations of H₂ in Orion, with the result that about 1900 L_⊙ are due to fluorescent emission while only 40 L_⊙ are due to thermal emission. From these numbers, we calculate that 1.3×10^3 HII regions similar to Orion would be required to account for the fluorescent emission we observe in NGC 253. This number of Orion-like HII regions is also nearly enough to account for the ionizing flux from NGC 253— 3×10^{49} s⁻¹ per Orion HII region (Bertoldi & Draine 1996) yields half the N_{L_{YC}} for the starburst.

These HII regions would provide 5.3×10^4 L_⊙ of thermal emission, leaving nearly all the thermal emission from NGC 253 unaccounted for. The deficit could be made up by thermal emission from diffuse shocks, either associated with supernova remnants or on larger scales. Graham, Wright, & Longmore (1987) and Burton et al. (1988) derive an H₂ luminosity in the supernova remnant IC 443 of ~ 70 L_⊙. Taking this to be the average luminosity per supernova remnant, and given the estimated supernova rate in NGC 253, the average H₂-emitting lifetime of the supernova remnants would have to be $\sim 6 \times 10^5$ years. This lifetime is implausibly long, particularly since at this age any supernova remnant in NGC 253 will have expanded and merged with the general hot interstellar medium. Instead, we suggest that much of the thermal H₂ arises from cloud-cloud collisions or other diffuse shocks (c.f. van der Werf et al. 1993), some of which

may be powered by mechanical energy released by supernovae and stellar winds. This possibility is supported by the differences in distribution of [Fe II] and H₂ emission in the position-velocity plots in Figure 8.

5.4. Nature of Weak-[O I] LINERs

Although the intrinsic [O II]/[O III]5007 line ratio is difficult to determine for NGC 253 because of the strong reddening, other, less reddening-dependent diagnostic optical line ratios indicate it is a transitional HII/weak-[O I] LINER. Filippenko & Terlevich (1992) use nebular models to demonstrate that this class of galaxy can be excited by hot stars, with $T \geq 45,000$ K. The locus of NGC 253 on the diagnostic plots of Filippenko & Terlevich falls even closer to their theoretical calculations than does the zone they indicate for typical weak-[O I] LINERs. Alternatively, it has been proposed that these LINERs are excited by shocks (e.g., Heckman 1980).

The strong arguments against the effective stellar temperature in NGC 253 being nearly as hot as 45,000 K are difficult to reconcile with the model of Filippenko & Terlevich. In fact, our data are difficult to reconcile with any model based on photoionization from a hard UV spectrum, since the indications of low stellar temperature also argue against a hard UV field from a mini-AGN or other source. Moreover, there are few other traces of a mini-AGN in this galaxy. For example, our measurement of Br γ shows the line to be narrow with no broad wings. On the extinction-free [O I]/H α vs. [Fe II] 1.64 μ m/Br γ diagnostic diagram, NGC 253 falls near the middle of the starburst locus (Alonso-Herrero et al. 1997). There is no hard X-ray source in the nucleus of the galaxy, and although there is a compact radio source (Turner & Ho 1985), it is of low luminosity.

It seems likely that the LINER-like characteristics of NGC 253 are produced by a mechanism other than photoionization. We have shown that the [Fe II] emission is likely to be produced directly in supernova remnants. Alonso-Herrero et al. (1997) demonstrate that NGC 253 falls approximately on the mixing line between HII regions and supernova remnants on the [O I]/H α vs [Fe II]/Br γ diagram. That is, the [O I] strength is also consistent with an origin predominantly in the same supernova remnants that produce the [Fe II], with additional H recombination emission from HII regions.

The influence of supernovae on the observed emission line spectrum of NGC 253 can be determined more quantitatively. We have determined an average supernova emission line spectrum by averaging the line strengths (normalized to H α) for 32 supernova remnants measured by Danziger & Leibowitz (1985), Fesen, Blair & Kirshner (1985), and Blair & Kirshner (1985). Similarly, an average ratio of [Fe II] 1.64 μ m/Br γ can be determined for supernovae measured by Oliva, Moorwood & Danziger (1989; 1990). Taking H α /Br γ = 103 from Case B, we find that [O I]/[Fe II] \sim 1.25. Relating these values through the H recombination lines is an essential step because of the differing geometries in the available optical and near infrared spectra. Nonetheless,

because of the relatively small amount of infrared data, the derived ratio is somewhat uncertain.

We can predict the optical spectrum from the infrared one with: 1.) the relations derived in the preceding paragraph; 2.) the total [Fe II] flux of $3.8 \times 10^{-12} \text{ erg s}^{-1} \text{ cm}^{-2}$ derived in Section 3.2; 3.) the total Br γ flux of $2.14 \times 10^{-12} \text{ erg s}^{-1} \text{ cm}^{-2}$ derived in Section 5.4; 4.) case B ratios for the H recombination lines; and 5.) standard nebular calculations for the relative strengths of photoionized lines in the optical (we have used the work of Shields & Kennicutt (1995), which includes the effects of dust in metal-rich HII regions). We assume a stellar temperature of 38,000 K (the lowest for which Shields & Kennicutt give calculations) and solar metallicity. We also use the [O I]/H α ratio for the Orion nebula to represent a typical HII region. The results of these predictions are summarized in Table 10.

The agreement between predicted and observed line ratios is well within the uncertainties. About 85% of the [O I] and half of the [O III] are excited in the supernovae remnants, whereas most of the [N II], [S II], and H recombination are excited by photoionization. Although the photoionized portion of the [O III] will decrease rapidly with decreasing stellar temperature, the large portion of shock-excited [O III] will maintain good agreement with the observations. If the intrinsic [O I]/[Fe II] ratio is a factor of 1.5 higher than we have used (which is within our guess of the errors), the agreement between predictions and observations is improved and the [O III]/H β ratio becomes almost independent of a decreased stellar temperature.

Thus, a combination of a metal-rich HII region photoionization model with the shocked optical line strengths predicted by assuming the [Fe II] is produced by supernovae provides a satisfactory fit to all the LINER-like characteristics of NGC 253. This fit involves no free parameters, other than those determined independently of the LINER characteristics. The Filippenko & Terlevich (1992) hot star photoionization model would predict that LINERs appear as a very early stage in a starburst. Instead, we suggest that the LINER characteristics emerge after the stars emitting most vigorously in the UV have died, so the HII region characteristics will fade sufficiently to reveal the supernova shock excitation.

The decay time for ionizing flux in a starburst is only a few million years, whereas the supernova rate is maintained for about 30 million years. Therefore, if the star-forming episodes in starbursts are typically short in duration, of order 20 million years, then there should be a significant population of objects in the transitional stage that produces LINER characteristics. In agreement with this conclusion, we found in §4.2 that starburst models with these characteristics give the best overall fit to the properties of NGC 253.

6. Conclusion

We have presented high-quality spectra of the nuclear region of NGC 253 in the J, H, and K bands. We have constructed a composite stellar spectrum and subtracted it from that of NGC 253 to obtain accurate measurements of faint emission lines free from the spectral structure due

to stellar absorptions. We have also presented J, H, and K_s -band images, narrow-band images in the lines of $\text{Br}\gamma$ and $\text{H}_2(1,0)\text{S}(1)$, spectra at $10.5\mu\text{m}$, and a high-resolution spectral map at $12.8\mu\text{m}$. We have used these data and data from the literature to perform a detailed study of the interstellar medium and nuclear starburst in NGC 253. All of the observed properties, from the radio through the X-ray, can be explained plausibly by a starburst. Specifically, we find:

- 1.) The density in the [Fe II]-emitting region is $\sim 5 \times 10^3 \text{ cm}^{-3}$, similar to that observed for [Fe II]-emitting regions in supernova remnants. The strength of the [Fe II] emission is consistent with the supernova rate estimated from radio observations and predicted by starburst models. Together, these results confirm that the [Fe II] is produced predominantly in the supernovae in the starburst.
- 2.) Roughly two thirds of the infrared H_2 luminosity is due to UV fluorescence. It is likely that significant fluorescent-excited components of H_2 emission in other starburst galaxies have been missed because the distribution of emission over many relatively faint lines makes detection difficult in spectra of modest resolution and signal to noise. If the Lyman continuum is produced by Orion-like HII regions, they would also come within a factor of ~ 2 of producing the fluorescent H_2 .
- 3.) From the MIR fine-structure lines of [S IV] and [Ne II], we find that the stars photoionizing the gas in NGC 253 have $T_{eff} < 37000 \text{ K}$, with $< 15\%$ of the ionizing flux coming from stars with $T > 40000 \text{ K}$. We also use an upper limit to $\text{HeI}(1.7)/\text{Br}10$ to place an upper limit on the stellar temperature of $\sim 37,000 \text{ K}$. These values are consistent with the temperature determination of $34,500 \pm 1,000\text{K}$ derived from far infrared fine structure lines by Carral et al. (1994).
- 4.) The optical line ratios in NGC 253 indicate it is a HII/weak-[O I] LINER and they are fitted well by the hot-star ($T \sim 45,000\text{K}$) photoionization models proposed for this type of active galaxy by Filippenko & Terlevich (1992). However, the stellar temperature determinations are inconsistent with the hot star model. The line ratios can also be fitted by a combination of a photoionization model for metal rich HII regions excited by stars of $\sim 38,000\text{K}$, and the shock excited spectrum of supernova explosions occurring at the rate measured in the starburst. These components fit NGC 253 with virtually no adjustment of free parameters. We suggest that many weak-[O I] LINERs can be explained in the same manner, rather than by the presence of a mini-AGN or by hot stars.
- 5.) We have used the infrared data to derive extinction-independent estimates of the primary boundary conditions for starburst models of NGC 253: mass, N_{LyC} , maximum stellar temperature, bolometric luminosity, and CO absorption depth.
- 6.) We find that IMF8, proposed by RLRT93 as the best-fitting for M 82, also provides a good fit to the properties of NGC 253 and suggests a starburst mass of $6 \times 10^7 M_{\odot}$. IMF3, which was assembled by RLRT93 to represent various representations of the local IMF, is not satisfactory although it cannot be ruled out as absolutely as for extreme galaxies like M 82 and NGC 1614. IMF8 is very similar to the modified Salpeter IMF that other workers have recently found gives

a good fit in starburst galaxy models. Due to the large variations or uncertainties in IMFs above $1 M_{\odot}$, it is no longer clear whether IMF3 is a meaningful representation of the local stellar population to be compared with those in starbursts.

7.) The model giving the best fit assumes that the star formation is extended over 20 to 30 million years. A portion of the supernovae is associated with stars formed near the beginning of the burst, while the ionizing flux arises from the most recently formed stars. The rate of star formation must have declined rapidly during the last roughly 5 million years, to account for the absence of very hot stars. This model is in agreement with our suggestion that a HII/weak-[O I] LINER can arise from a late phase of a starburst.

This research has made use of the NASA/IPAC extragalactic database (NED) which is operated by the Jet Propulsion Laboratory, Caltech, under contract with the National Aeronautics and Space Administration. NSO/Kitt Peak FTS data used here were produced by NSF/NOAO. The authors would like to thank C. A. Kulesa, J. H. Lacy, K. Luhman, R. Mauersberger, and H.-W. Rix for useful discussions. We would like to thank NSF for support through grants AST91-16442 and AST95-29190. DMK acknowledges support from NSF grants AST90-20292 (Texas) and AST94-53354 (Wyoming). We thank the anonymous referee and our editor, Steven Willner, for comments which improved this paper.

Table 1. NGC 253 Aperture Photometry

aperture(")	m_J	m_H	m_K	$J - H$	$H - K$
3	11.55	10.41	9.51	1.14	0.90
6	10.36	9.19	8.44	1.17	0.74
12	9.34	8.25	7.56	1.09	0.69
15	9.05	7.96	7.30	1.09	0.66
2.4×12	10.41	9.21	8.45	1.20	0.76

Note. — Aperture sizes are diameters of circular apertures except for the $2.4 \times 12''$ aperture which was used to calibrate the spectra as described in the text. Typical statistical uncertainties are 2% - 5%.

Table 2. Summary of Starburst Parameters

Parameter	Value
Mass	$\ll 2.1 \times 10^8 M_\odot$
L_{Bol}	$1.1 \times 10^{10} L_\odot$
M_K	-20.4
$\log N_{\text{LyC}}$	> 53.0
SNR	0.03 yr^{-1}
CO	0.20

Table 3. Hydrogen Recombination Line Measurements

Line	$\lambda_{vac}(\mu\text{m})$	Ratio to Br γ	
		Observed	Case B
Pa β	1.2822	1.66 ± 0.10	5.58
Br13	1.6114	0.10 ± 0.03	0.14
Br12	1.6412	...	0.18
Br11	1.6811	0.12 ± 0.03	0.24
Br10	1.7367	0.26 ± 0.05	0.32
Br δ	1.9451	0.61 ± 0.04	0.65
Br γ	2.1661	1.00	1.00

Note. — No corrections for extinction have been made. The flux in Br γ is $2.59 \pm 0.10 \times 10^{-13}$ erg s $^{-1}$ cm $^{-2}$ in a $2''.4 \times 12''$ aperture. The Case B values were derived from Hummer & Storey (1987), for $n = 10^2$ cm $^{-3}$, $T = 5000$ K.

Table 4. [Fe II] Lines

Transition	$\lambda_{vac}(\mu\text{m})$	Ratio to $\lambda 1.644\mu\text{m}$
$a^6 D_{9/2} - a^4 D_{7/2}$	1.2570	0.68 ± 0.04
$a^6 D_{3/2} - a^4 D_{3/2}$	1.2791	0.04 ± 0.01
$a^6 D_{5/2} - a^4 D_{5/2}$	1.2947	0.13 ± 0.03
$a^6 D_{7/2} - a^4 D_{7/2}$	1.3209	0.18 ± 0.02
$a^4 F_{9/2} - a^4 D_{5/2}$	1.5339	0.13 ± 0.03
$a^4 F_{9/2} - a^4 D_{7/2}$	1.6439	1.00
$a^4 F_{7/2} - a^4 D_{5/2}$	1.6774	0.06 ± 0.02

Note. — No correction has been made for extinction. The flux in the $\lambda 1.644\mu\text{m}$ line in a $2''.4 \times 12''$ aperture is $3.56 \pm 0.18 \times 10^{-13}$ erg s $^{-1}$ cm $^{-2}$.

Table 5. He Lines

Transition	$\lambda_{vac}(\mu\text{m})$	$10^{-14} \text{ erg s}^{-1} \text{ cm}^{-2}$
$3P - 4D$	1.7007	< 1.0
$2S - 2P$	2.0587	9.38 ± 1.1

Note. — These fluxes were extracted from a $2''.4 \times 12''$ aperture and are uncorrected for extinction.

Table 6. Velocity gradients of spectral features

Feature	gradient ($\text{km s}^{-1} / ''$)
$\text{Br}\gamma$	7.4 ± 0.4
H_2	7.7 ± 0.4
$\text{CO}(2,1)$	7.5 ± 0.9

Note. — These numbers are not corrected for inclination.

Table 7. Absorption features

Species	$\lambda_{vac}(\mu\text{m})$	$W_\lambda(\text{\AA})$
MgI	1.4882	1.6
MgI	1.5048	5.5
$^{12}\text{CO}(3,0)$	1.5582	4.0
MgI	1.5770	1.1
$^{12}\text{CO}(4,1)$	1.5780	5.6
FeI	1.5823	3.4
SiI	1.5893	4.6
SiI	1.5964	3.3
$^{12}\text{CO}(5,2)$	1.5982	3.6
$^{12}\text{CO}(6,3)$	1.6189	7.0
$^{12}\text{CO}(8,5)$	1.6618	2.2
AlI	1.6755	3.1
$^{12}\text{CO}(9,6)$	1.6840	4.3
$^{12}\text{CO}(10,7)$	1.7067	2.5
MgI	1.7146	2.3
FeI	1.7307	1.6
SiI	1.7332	3.0
FeI	2.0704	1.0
MgI	2.1066	1.2
AlI	2.1170	1.4
SiI	2.1360	1.4
NaI	2.207	3.2
FeI	2.2263	2.0
CaI	2.2631	3.3
CaI	2.2657	1.8
MgI	2.2814	1.1
$^{12}\text{CO}(2,0)$	2.2935	13.1
$^{12}\text{CO}(3,1)$	2.3227	16.4
$^{13}\text{CO}(2,0)$	2.3448	10.8
$^{12}\text{CO}(4,2)$	2.3525	16.4
$^{13}\text{CO}(3,1)$	2.3739	13.0
$^{12}\text{CO}(5,3)$	2.3830	17.1

Table 8. H₂ Line Fluxes

Transition	$\lambda_{vac}(\mu\text{m})$	Ratio to (1,0)S(1)				
		Obs.	Dered.	Fluor.	Therm.	Mix
(5,3)Q(1)	1.4929	< 0.1	< 0.18	0.43	1.0×10^{-4}	0.11
(4,2)O(3)	1.5099	< 0.1	< 0.18	0.42	7×10^{-4}	0.11
(6,4)Q(1)	1.6015	< 0.15	< 0.24	0.33	1.3×10^{-4}	0.08
(5,3)O(3)	1.6135	< 0.15	< 0.23	0.38	9×10^{-5}	0.10
(6,4)O(3)	1.7326	< 0.15	< 0.20	0.31	1×10^{-5}	0.08
(1,0)S(3)	1.9576	0.89 ± 0.08	0.99 ± 0.09	0.67	1.02	0.93
(2,1)S(4)	2.0041	0.18 ± 0.02	0.19 ± 0.02	0.12	0.02	0.05
(1,0)S(2)	2.0338	0.36 ± 0.05	0.38 ± 0.05	0.50	0.38	0.41
(2,1)S(3)	2.0735	0.26 ± 0.06	0.27 ± 0.06	0.35	0.08	0.15
(1,0)S(1)	2.1218	1.00	1.00	1.00	1.00	1.00
(2,1)S(2)	2.1542	0.20 ± 0.04	0.20 ± 0.04	0.28	0.04	0.09
(1,0)S(0)	2.2233	0.30 ± 0.03	0.28 ± 0.03	0.46	0.21	0.27
(2,1)S(1)	2.2477	0.21 ± 0.02	0.20 ± 0.02	0.56	0.08	0.21
(2,1)S(0)	2.3556	< 0.1	< 0.09	0.26	0.02	0.08
(3,2)S(1)	2.3865	< 0.1	< 0.09	0.29	5.8×10^{-3}	0.08
(1,0)Q(1)	2.4066	0.79 ± 0.16	0.68 ± 0.14	0.99	0.70	0.77
(1,0)Q(2)	2.4134	0.34 ± 0.07	0.29 ± 0.06	0.51	0.23	0.31
(1,0)Q(3)	2.4237	0.75 ± 0.15	0.64 ± 0.13	0.70	0.70	0.70
(1,0)Q(4)	2.4375	0.20 ± 0.04	0.17 ± 0.03	0.28	0.21	0.23

Note. — The flux in the (1,0)S(1) line is $1.21 \pm 0.07 \times 10^{-13}$ erg s⁻¹ cm⁻² (uncorrected for extinction) in a 2''.4×12'' aperture.

Table 9. H₂ rotational excitation temperatures

Vibrational Level	Rotational Levels	Rotational Excitation Temperature (K)
1	0,2	1350 ± 229
	1,3	1921 ± 175
2	1,3	3528 ± 860

Table 10. Predicted optical line ratios

ratio	predicted	observed	ref.
[O I]/H α	0.026	0.044	1
[N II]/H α	0.78	0.78	1
[S II]/H α	0.45	0.40	1
[O III]/H β	0.49	0.47	2

Note. — (1) Armus, Heckman, & Miley 1989; (2) Tadhunter et al. 1993.

REFERENCES

- Aannestand, P. 1989, *ApJ*, 338, 162
- Aaronson, M. 1977, Ph.D. thesis, Harvard Univ.
- Achtermann, J.M. 1994, PhD thesis, University of Texas
- Alonso-Herrero, A., Rieke, M. J., Rieke, G. H., Ruiz, M. 1997, *ApJ*, in press
- Anantharamaiah, K. R. & Goss, W. M. 1996, *ApJ*, 466, L13
- Antonucci, R. R. J. & Ulvestad, J. S. 1988, *ApJ*, 330, L97
- Armus, L., Heckman, T. M., & Miley, G. K. 1989, *ApJ*, 347, 727
- Arnaboldi, M., Capaccioli, M., Cappellaro, E., Held, E. V., & Koribalski, B. 1995, *AJ*, 110, 199
- Arnett, D. W. 1978, *ApJ*, 218, 1008
- Bautista, M. A. & Pradhan, A. K. 1996, *A&AS*, 115,551
- Beck, S. C. & Beckwith, S. V. 1984, *MNRAS*, 207, 671
- Bekki, K. 1995, *MNRAS*, 276, 9
- Bertoldi, F. & Draine, B. T. 1996, *ApJ*, 458, 222
- Black, J. H., & van Dishoeck, E. F. 1987, *ApJ*, 322, 412
- Blair, W. P. & Kirshner, R. P. 1985, *ApJ*, 289, 582
- Burton, M. G., Geballe, T. R., Brand, P. W. J. L., & Webster, A. S. 1988, *MNRAS*, 231, 617
- Calzetti, D., Kinney, A. L, & Storchi-Bergmann, T. 1996, *ApJ*, 458, 132
- Canzian, B., Mundy, L. G., & Scoville, N. Z. 1988, *ApJ*, 333, 157
- Carral, P., Hollenbach, D. J., Lord, S. D., Colgan, S. W. J., Haas, M. R., Rubin, R. H., & Erickson, E. F. 1994, *ApJ*, 423, 223
- Colina, L. & Pérez-Olea, D. 1992, *MNRAS*, 259, 709
- Condon, J. J., & Yin, Q. F. 1990, *ApJ*, 357, 97
- Conti, P. S., Leitherer, C., & Vacca, W. D. 1996, *ApJ*, 461, L87
- Courteau, S. 1994, *A Compilation of the Faint UKIRT Standards*
- Danziger, I. J. & Leibowitz, E. M. 1985, *MNRAS*, 216, 365
- Danziger, I. J., Murdin, P. G., Clark, D. H., & D’Odorico, S. 1979, *MNRAS*, 186, 555
- de Vaucouleurs, G. 1978, *ApJ*, 224, 710
- Devereux, N. A., Becklin, E. E., & Scoville, N. A. 1987, *ApJ*, 312, 529
- Doyon, R., Joseph, R. D., & Wright, G. S. 1994, *ApJ*, 421, 101
- Engelbracht, C. W., Rieke, M. J., Rieke, G. H., & Latter, W. B. 1996, *ApJ*, 467, 227 (ERRL96)
- Fabbiano, G. 1988, *ApJ*, 330, 672

- Fabbiano, G. 1996, in Proc. Röntgenstrahlung from the Universe, ed. Zimmerman, Trümper, Yorke, MPE Report, 263, 347
- Ferland, G.J. 1993, U. of Kentucky Physics Department Internal Report
- Fesen, R. A., Blair, W. P., & Kirshner, R. P. 1985, ApJ, 292, 29
- Filippenko, A. V. & Terlevich, R. 1992, ApJ, 397, L79
- Forbes, D. A. & Depoy, D. L. 1992, A&A, 259, 97
- Forbes, D. A. & Ward, M. J. 1993, ApJ, 416, 150
- Forbes, D. A., Ward, M. J., DePoy, D. L., Boisson, C., & Smith, M. S. 1992, MNRAS, 254, 509
- Forbes, D. A., Ward, M. J., Rotaciuc, V., Blietz, M., Genzel, R., Drapatz, S., van der Werf, P. P., & Krabbe, A. 1993, ApJ, 406, L11
- Frogel, J. A., Persson, S. E., Aaronson, M., & Mathews, K. 1978, ApJ, 220, 75
- Gear, W. K., Gee, G., Robson, E. I., Ade, P. A. R., & Duncan, W. D. 1986, MNRAS, 219, 19p
- Goldader, J. D., Joseph, R. D., Doyon, R., & Sanders, D. B. 1997, ApJS, in press
- Graham, J. R., Wright, G. S., & Longmore, A. J., 1987, ApJ, 313, 847
- Greenhouse, M. A., Woodward, C. E., Thronson, H. A., Rudy, R. J., Rossano, G. S., Erwin, P., & Puetter, R. C. 1991, ApJ, 383, 164
- Heckman, T. M., 1980, A&A, 87, 152
- Heckman, T. M., 1997, preprint, to be published in the proceedings of the conference ‘Origins’, Ed. C. Woodward and J.M. Shull, (PASP)
- Heckman, T. M., Armus, L., & Miley, G. K. 1990, ApJS, 74, 833
- Hummer, D. G. & Storey, P. J. 1987, MNRAS, 224, 801
- Keto, E., Ball, R., Skinner, C., Arens, J., Jernigan, G., Meixner, M., & Graham, J. 1994, Exp. Ast., 3, 161
- Kleinmann, S. G., & Hall, D. N. B. 1986, ApJS, 62, 501
- Kormendy, J., & Richstone, D. 1992, ApJ, 393, 559
- Koornneef, J. & Israel, F. P. 1996, New Astron., 1, 271
- Krügel, E., Chini, R., Klein, U., et al. 1990, A&A, 240, 232
- Kulesa, C. A., Black, J. H., Rieke, G. H., & Rieke, M. J. 1998, submitted to ApJ
- Lacy, J.H., & Achtermann, J.M. 1994, in Infrared Astronomy with Arrays, I. McLean (ed.), p.85
- Lacy, J.H., Achtermann, J.M., Bruce, D.E., Lester, D.F., Arens, J.F., Peck, M.C., & Gaalema, S.D. 1989, PASP, 101, 1166
- Lehnert, M. D. & Heckman, T. M. 1995, ApJS, 97, 89
- Leitherer, C. & Heckman, T. M. 1995, ApJS, 96, 9

- Leitherer, C., Vacca, W. D., Conti, P. S., Filippenko, A. V., Robert, C., Sargent, W. L. W. 1996, ApJ, 465, 717
- Livingston, W. & Wallace, L. 1991, NSO Tech. Rep. 91-001 (Tucson: NOAO)
- Luhman, M. L., Jaffe, D. T., Keller, L. D., & Pak, S. 1994, ApJ, 436, L185
- Maeder, A. 1992. Private communication
- Maloney, P. R. & Black, J. H. 1988, ApJ, 325, 389
- Mauersberger, R., Henkel, C., Wielebinski, R., Wiklind, T., & Reuter, H.-P. 1996, A&A, 305, 421
- McCarthy, P. J., Heckman, T., & van Breugel, W. 1987, AJ, 92, 264
- McLeod, K. K., Rieke, G. H., Rieke, M. J., & Kelly, D. M. 1993, ApJ, 412, 111
- Muñoz-Tuñon, C., Vilchez, J. M., & Castañeda, H. O. 1993, A&A, 278, 364
- Nussbaumer, H., & Storey, P. J. 1988, A&A, 193, 327
- Oliva, E., Moorwood, A. F. M., & Danziger, I. J. 1989, A&A, 214, 307
- Oliva, E., Moorwood, A. F. M., & Danziger, I. J. 1990, A&A, 240, 453
- Origlia, L., Moorwood, A. F. M., & Oliva, E. 1993, A&A, 280, 536
- Paglione, T. A. D., Marscher, A. P., Jackson, J. M., & Bertsch, D. L. 1996, ApJ, 460, 295
- Pence, W. D. 1981, ApJ, 247, 473
- Peng, R., Zhou, S., Whiteoak, J. B., Lo, K. Y., & Sutton, E. C. 1996, ApJ, 470, 821
- Pompea, S. M. & Rieke, G. H. 1990, ApJ, 356, 416
- Prada, F., Manchado, A., Canzian, B., Peletier, R. F., McKeith, C. D., & Beckman, J. E. 1996, ApJ, 458, 537
- Pradhan, A. K., & Zhang, H. L. 1993, ApJ, 409, L77
- Ptak, A. Serlemitsos, P., Yaqoob, T., Mushotzky, R. & Tsuru, T. 1997, AJ, 113, 1286
- Puxley, P. J. 1991, MNRAS, 249, 11p
- Puxley, P. J., & Brand, P. W. J. L. 1995, MNRAS, 274, L77
- Puxley, P. J., Mountain, C. M., Brand, P. W. J. L., Moore, T. J. T., & Nakai, N. 1997, ApJ, 485, 143
- Ramsay, S. K., Chrysostomou, A., Geballe, T. R., Brand, P. W. J. L., & Mountain, M. 1993, MNRAS, 263, 695
- Rice, W., Lonsdale, C. J., Soifer, B. T., Neugebauer, G., Koplan, E. L., Lloyd, L. A., de Jong, T., & Habing, H. J. 1988, ApJS, 68, 91
- Rieke, G. H., & Lebofsky, M. J. 1978, ARA&A, 1979, 17, 477
- Rieke, G. H., & Lebofsky, M. J. 1985, ApJ, 288, 618
- Rieke, G. H., Lebofsky, M. J., Thompson, R. I., Low, F. J., & Tokunaga, A. T. 1980, ApJ, 238, 24

- Rieke, G. H., Lebofsky, M. J., & Walker, C. E. 1988, *ApJ*, 325, 679
- Rieke, G. H., Loken, K., Rieke, M. J., & Tamblyn, P. 1993, *ApJ*, 412, 99 (RLRT93)
- Rieke, G. H. & Low, F. J. 1975, *ApJ*, 197, 17
- Roche, P.F., & Aitken, D.K. 1985, *MNRAS*, 213, 789
- Roche, P. F., Aitken, D. K., Smith, C. H., & Ward, M. J. 1991, *MNRAS*, 248, 606
- Sams, B. J., III, Genzel, R., Eckart, A., Tacconi-Garman, L., & Hofmann, R. 1994, *ApJ*, 430, L33
- Satyapal, S., Watson, D. M., Pipher, J. L., Forrest, W. J., Greenhouse, M. A., Smith, H. A., Fischer, J., & Woodward, C. E. 1997, *ApJ*, 483, 148
- Scalo, J. 1986, *Fund. Cosmic Phys.*, 11, 3
- Scalo, J. 1998, in *Proc. 38th Herstmonceux Conference on Stellar IMF*, ed. Gilmore, Parry, Ryan Schinnerer, E., Eckart, A., Quirrenbach, A., Böker, T., Tacconi-Garman, L. E., Krabbe, A., & Sternberg, A. 1997, *ApJ*, 488, 174
- Scoville, N. Z., Soifer, B. T., Neugebauer, G., Young, J. S., Matthews, K., & Yerka, J. 1985, *ApJ*, 289, 129
- Shields, J. C. & Kennicutt, R. C. 1995, *ApJ*, 454, 807
- Shier, L. M., Rieke, M. J., & Rieke, G. H. 1994, *ApJ*, 433, L9
- Shier, L. M., Rieke, M. J., & Rieke, G. H. 1996, *ApJ*, 470, 222
- Smith, B. J. & Harvey, P. M. 1996, *ApJ*, 468, 139
- Spinoglio, L., Malkan, M., Rush, B., Carrasco, L., & Recillas-Cruz, E. 1995, *ApJ*, 453, 616
- Tadhunter, C. N., Morganti, R., di Serego Alighieri, S., Fosbury, R. A. E., & Danziger, I. J. 1993, *MNRAS*, 259, 709
- Telesco, C. M. 1988, *ARA&A*, 26, 343
- Telesco, C. M., Dressel, L. L., & Wolstencroft, R. D. 1993, *ApJ*, 414, 120
- Thronson, H. A., & Greenhouse, M. A. 1988, *ApJ*, 327, 671
- Tremaine, S., Richstone, D. O., Byun, Y., Dressler, A., Faber, S. M., Grillmair, C., Kormendy, J., & Lauer, T. R. 1994, *AJ*, 107, 634
- Turner, J. L. & Ho, P. T. P. 1983, *ApJ*, 268, L79
- Turner, J. L. & Ho, P. T. P. 1985, *ApJ*, 299, L77
- Ulvestad, J. S. & Antonucci, R. R. J. 1991, *AJ*, 102, 875
- Ulvestad, J. S. & Antonucci, R. R. J. 1994, *ApJ*, 424, L29
- Ulvestad, J. S. & Antonucci, R. R. J. 1997, *ApJ*, 488, 621
- Van Buren, D. & Greenhouse, M. A. 1994, *ApJ*, (431, 640)

- van der Werf, P. P., Genzel, R., Krabbe, A., Blietz, M., Lutz, D., Drapatz, S., Ward, Martin J., Forbes, D. A., 1993, *ApJ*, 405, 522
- Vanzi, L. & Rieke, G. H. 1997, *ApJ*, 479, 694
- Vanzi, L., Rieke, G. H., Martin, C. L., & Shields, J. C. 1996, *ApJ*, 466, 150
- Wada, K. & Habe, A. 1992, *MNRAS*, 258, 82
- Watson, A. M., Gallagher, J. S., III, Holtzman, J. A., Hester, J. J., Mould, J. R., Ballester, G. E., Burrows, C. J., Casertano, S., Clarke, J. T., Crisp, D., Evans, R., Griffiths, R. E., Hoessel, J. G., Scowen, P. A., Stapelfeldt, K. R., Trauger, J. T., Westphal, J. A., *AJ*, 112, 534
- Williams, D. M., Thompson, C. L., Rieke, G. H., & Montgomery, E. F. 1993, *S.P.I.E.*, 1946, 482
- Witt, A. N., Thronson, H. A., & Capuano, J. M. 1992, *ApJ*, 393, 611

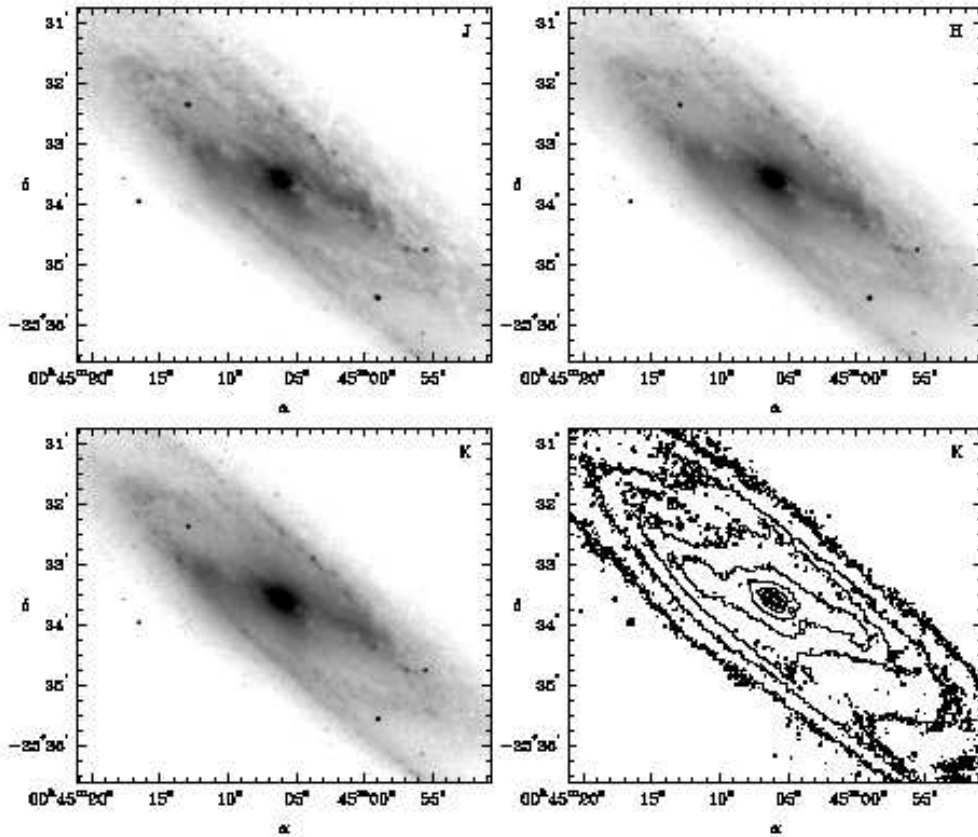


Fig. 1.— Greyscale images of NGC 253 in J, H, and K bands, plus a contour map at K. The display ranges are 17 to 20, 16.2 to 19.2, 16 to 19, and 14 to 19.4 magnitudes in the J, H, K, and K-contour images, respectively.

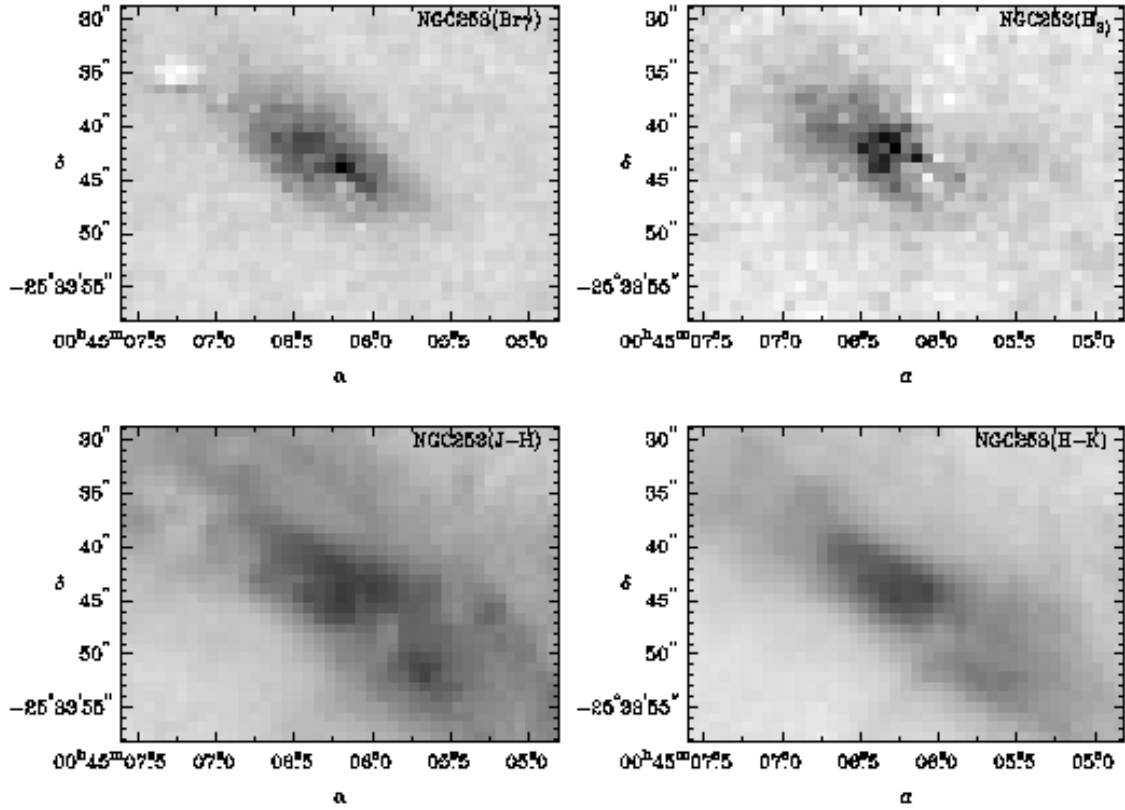


Fig. 2.— Greyscale images of the nuclear region of NGC 253 in narrow, continuum-subtracted bands centered at the lines of H $_2$ (1,0)S(1) and Br γ , plus $J - H$ and $H - K$ color maps of the same region. The display range is 0.6 to 1.5 magnitudes for the $J - H$ image and 0.1 to 1.2 magnitudes for the $H - K$ image.

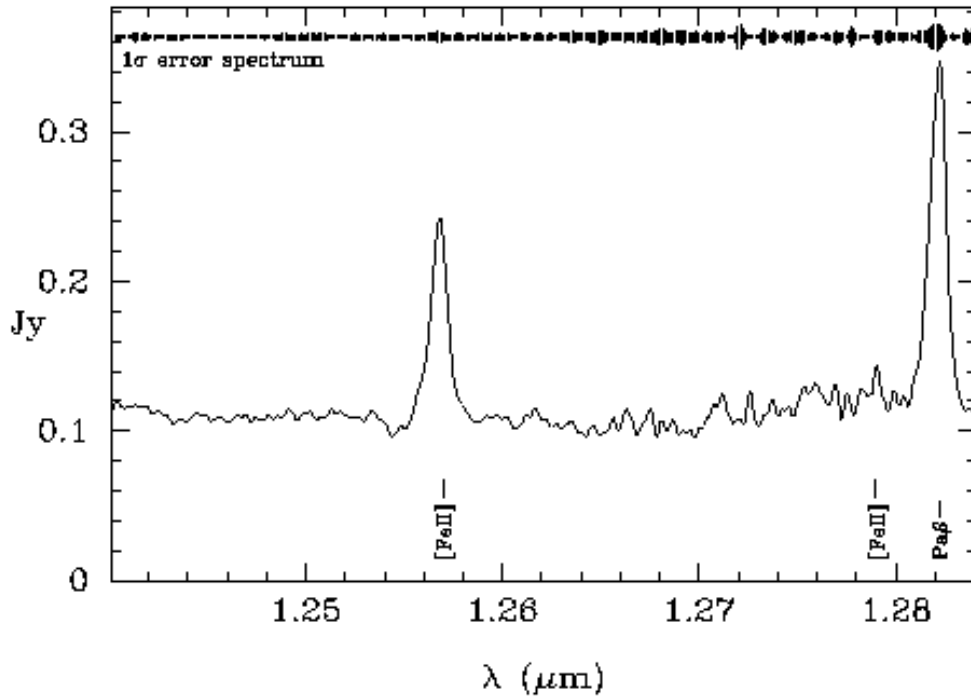


Fig. 3.— High-resolution J-band spectrum of NGC 253. The slit was oriented along the plane of the galaxy and was $2''.4$ wide. The spectrum shown here is the sum of the central $12''$. The spectrum was flux-calibrated as described in the text and has been shifted to zero velocity. Above the flux spectrum is plotted the 1-sigma error spectrum.

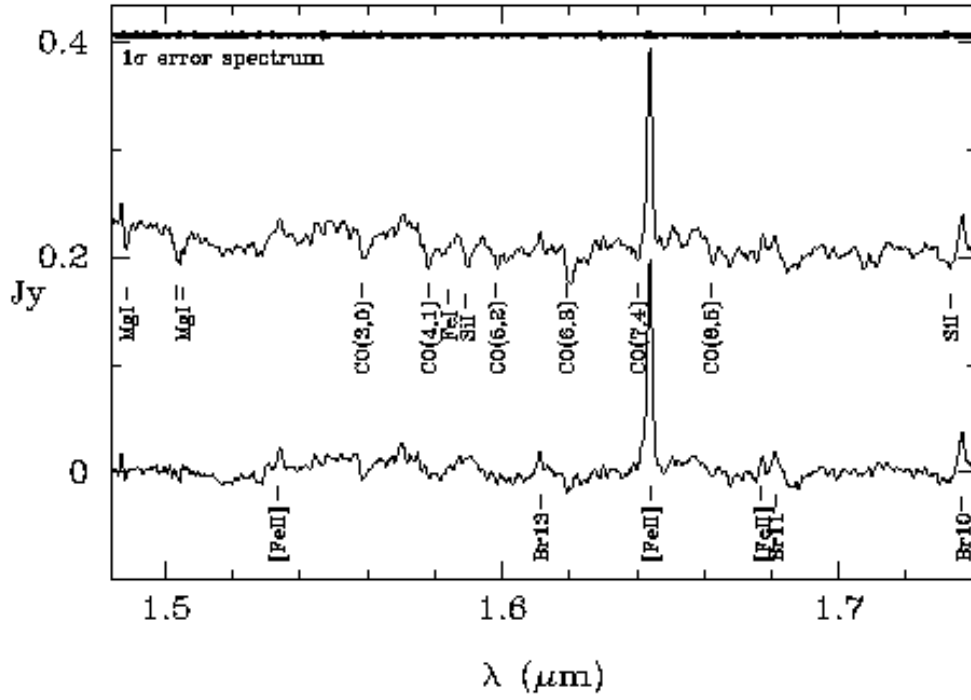


Fig. 4.— High-resolution H-band spectrum of NGC 253. Details as for the J-band spectrum. The lower spectrum is the result of subtracting a stellar continuum spectrum (produced by combining several late-type stellar spectra as described in the text) from the galaxy spectrum.

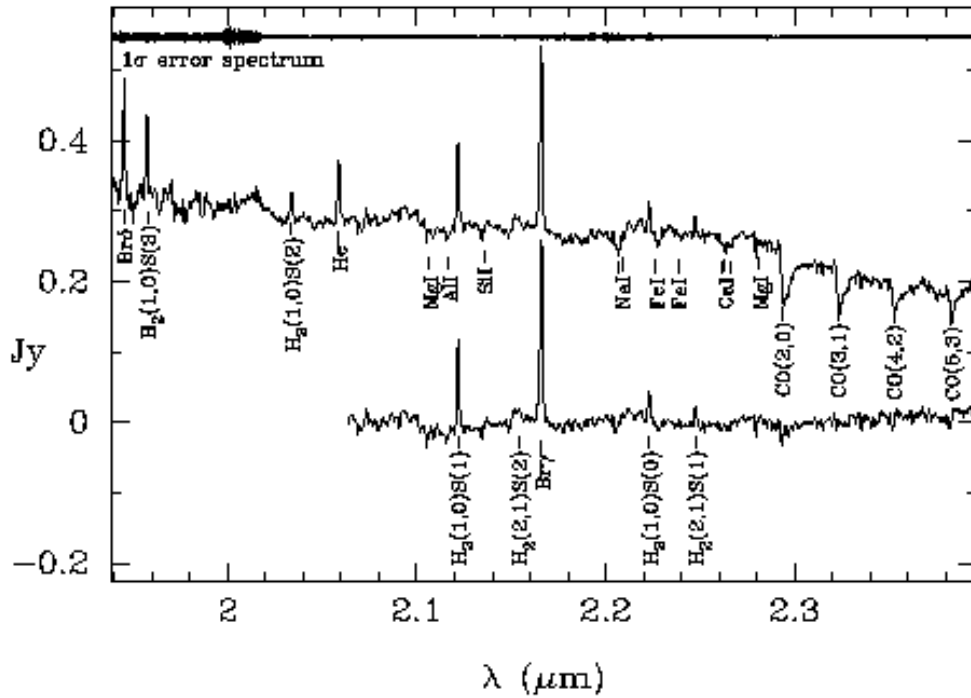


Fig. 5.— High-resolution K-band spectrum of NGC 253. Details as for J-band spectrum, and a stellar continuum subtraction has been performed as for the H-band spectrum. The region shortward of $2.06\mu\text{m}$ contains few significant stellar absorptions and so many of our stellar spectra do not cover this region. Note that the error spectrum indicates the spectrum is significantly noisier shortward of $2.02\mu\text{m}$, where the atmospheric transmission becomes poor.

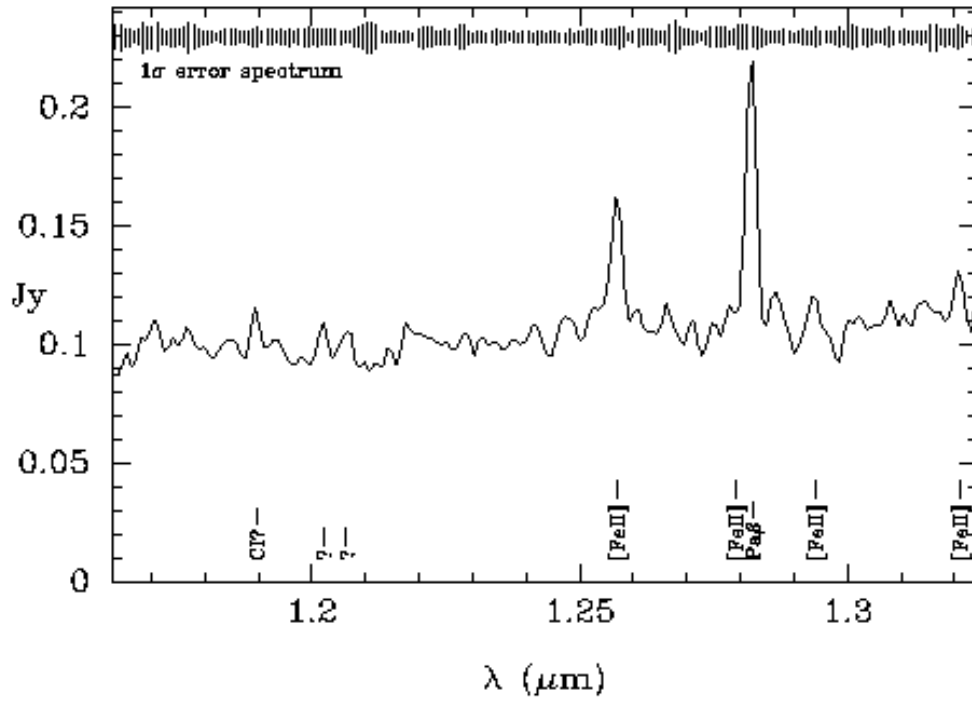


Fig. 6.— Low-resolution J-band spectrum of NGC 253. Details as for the high-resolution spectrum.

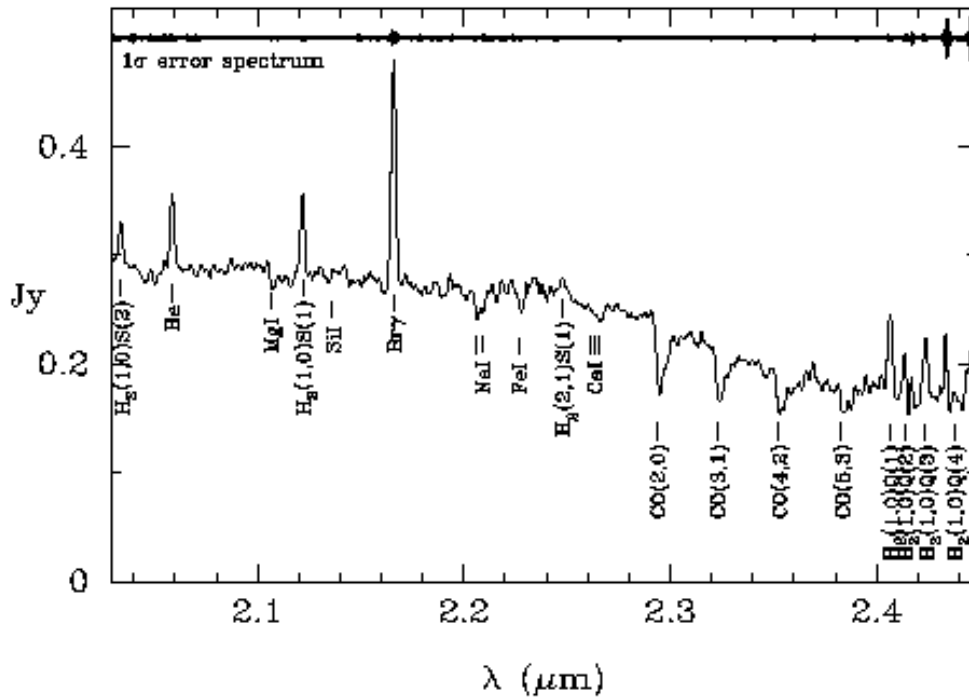


Fig. 7.— Low-resolution K-band spectrum of NGC 253. Details as for J-band spectrum. The apparent emission features beyond $2.4\mu\text{m}$ that are not labeled as H₂ lines correspond to regions of poor atmospheric transmission, as indicated by the spikes in the error spectrum at those points.

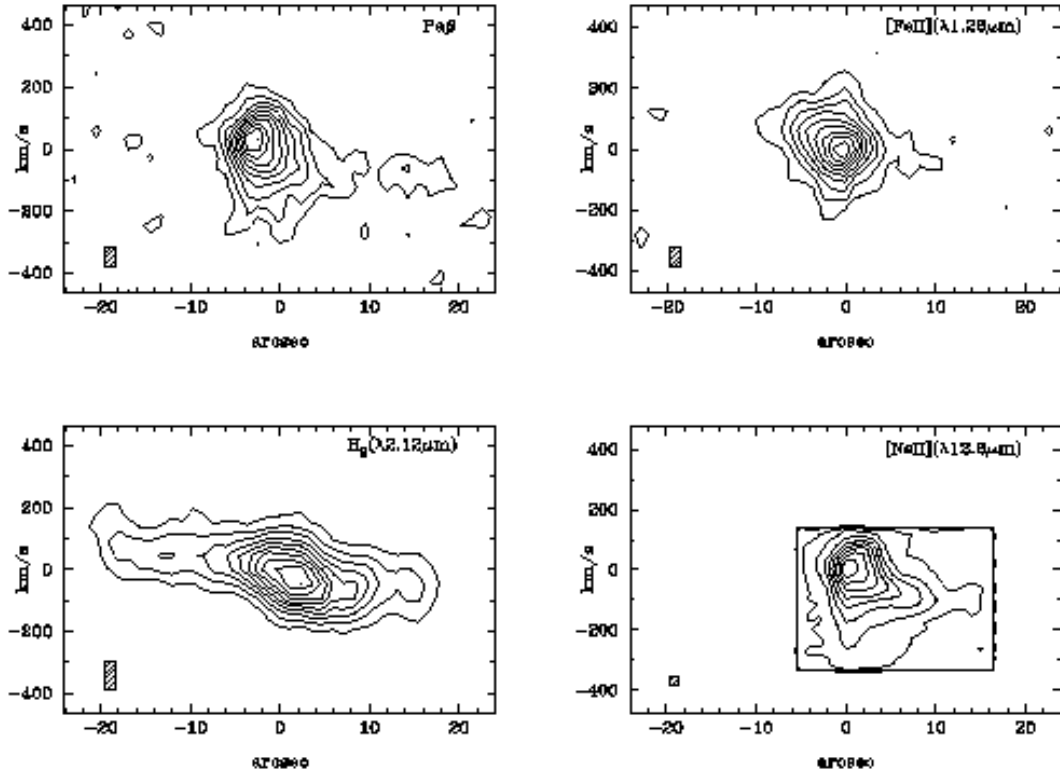


Fig. 8.— Position-velocity plots along the major axis for several strong lines. NE is on the right and SW on the left. In each case, the upper 90% of the contours are plotted. The hatched region in the lower-left-hand corner of each plot indicates the size of a resolution element along the spatial and dispersion axes. The [Ne II] observations were obtained in the 22'' boxed region shown on the plot.

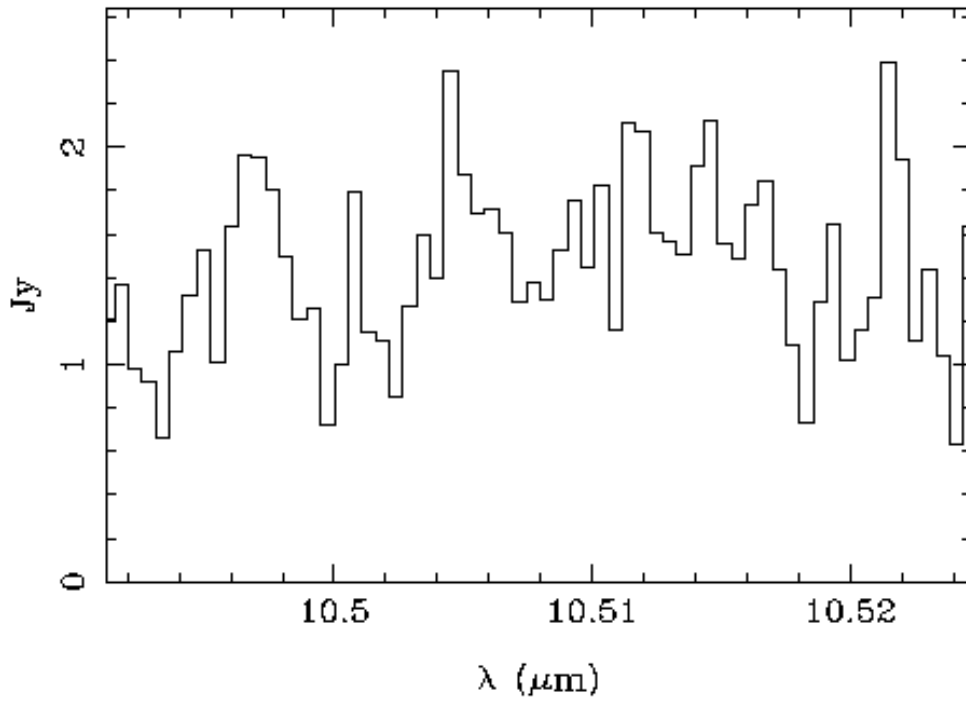


Fig. 9.— MIR spectrum of the central region of NGC 253, used to determine an upper limit to the [S IV] flux. See details in Section 2.4.

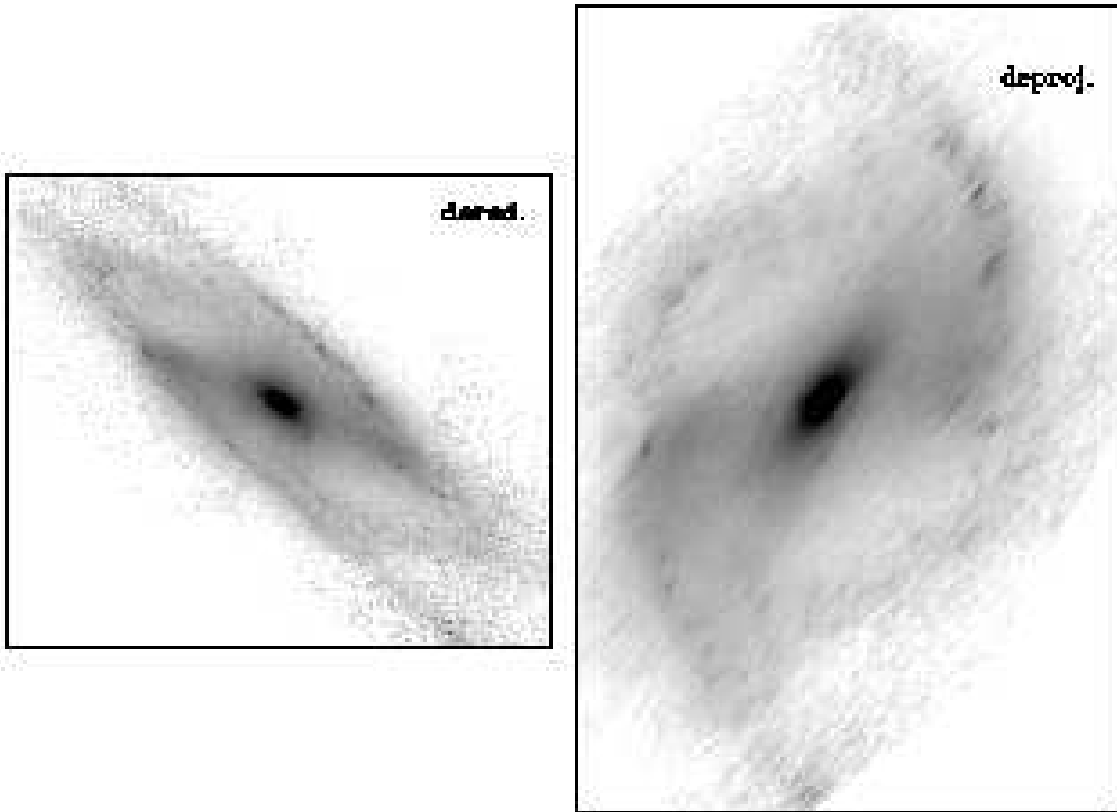


Fig. 10.— K-band image of NGC 253 dereddened as described in the text, then deprojected along the minor axis to determine how the galaxy would appear if viewed face on. The images are presented on a logarithmic intensity scale. The scale and orientation of the images are the same as Figure 1.

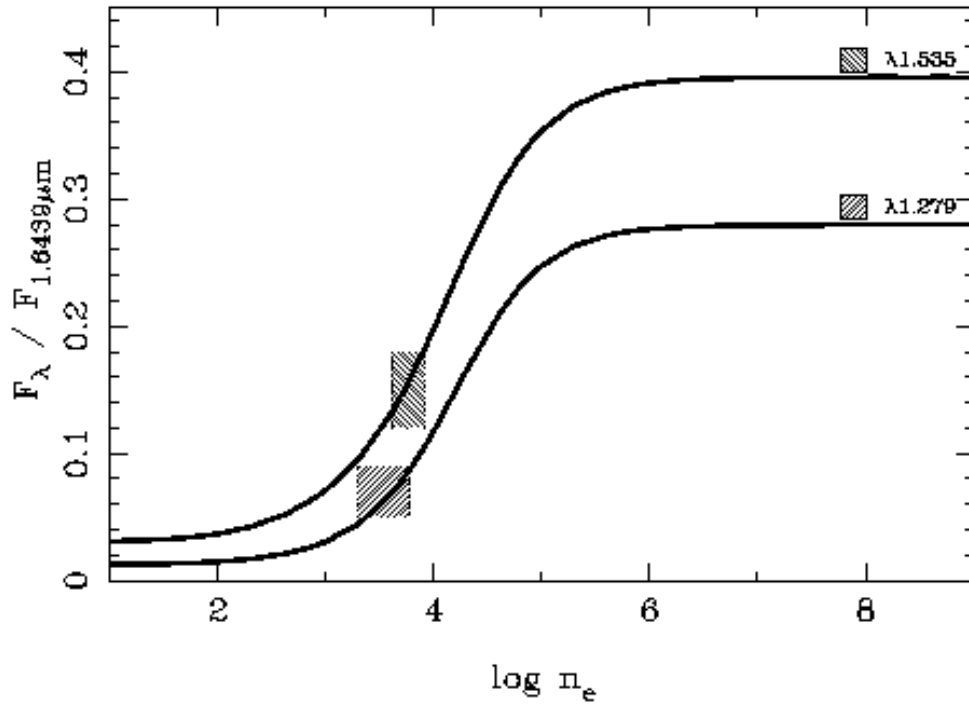


Fig. 11.— Plot of [Fe II] line ratios as a function of density. The line ratios have been corrected for the extinction derived in §3.1. The range allowed by the observations is indicated by the shaded regions. The diagnostic lines we have used here indicate that $\log(n_e)$ in the [Fe II] -emitting region is 3.7 ± 0.13 .

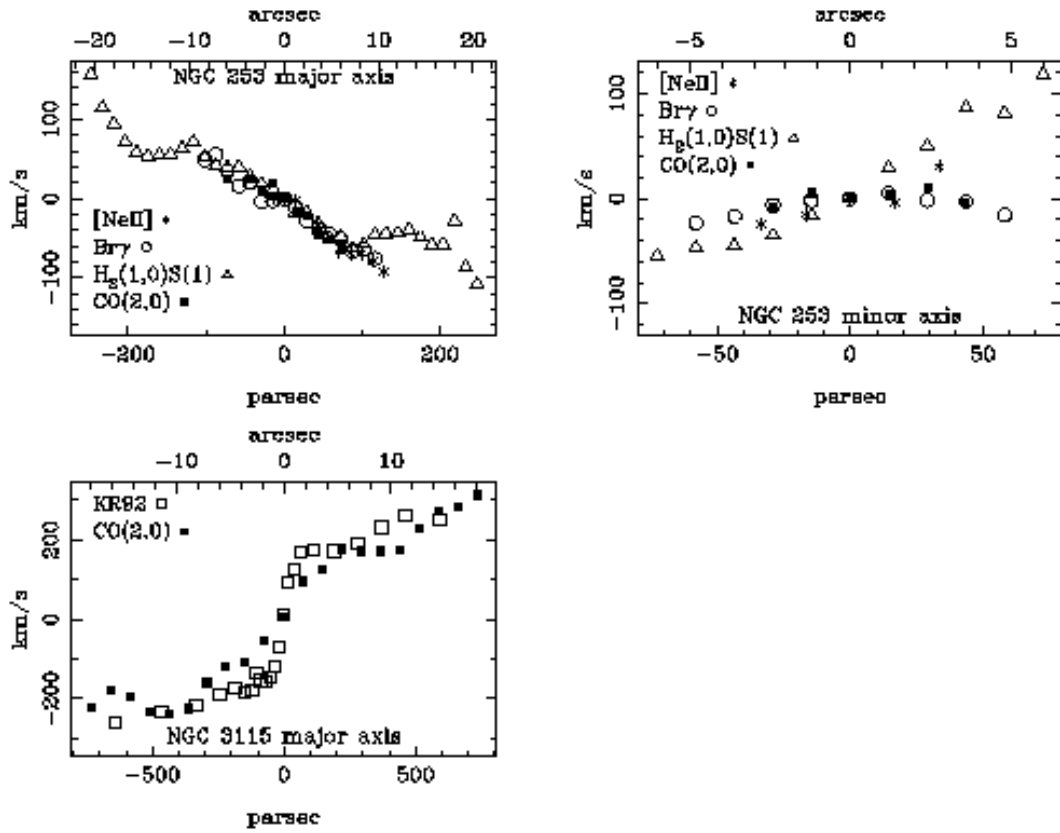


Fig. 12.— Rotation curves for NGC 253 and NGC 3115. NE is on the right and SW to the left in the NGC 253 major-axis plot while SE is on the right and NW to the left in the minor-axis plot. The linear dimensions have been determined by assuming distances of 2.5 Mpc and 8.4 Mpc, respectively, for NGC 253 and NGC 3115.

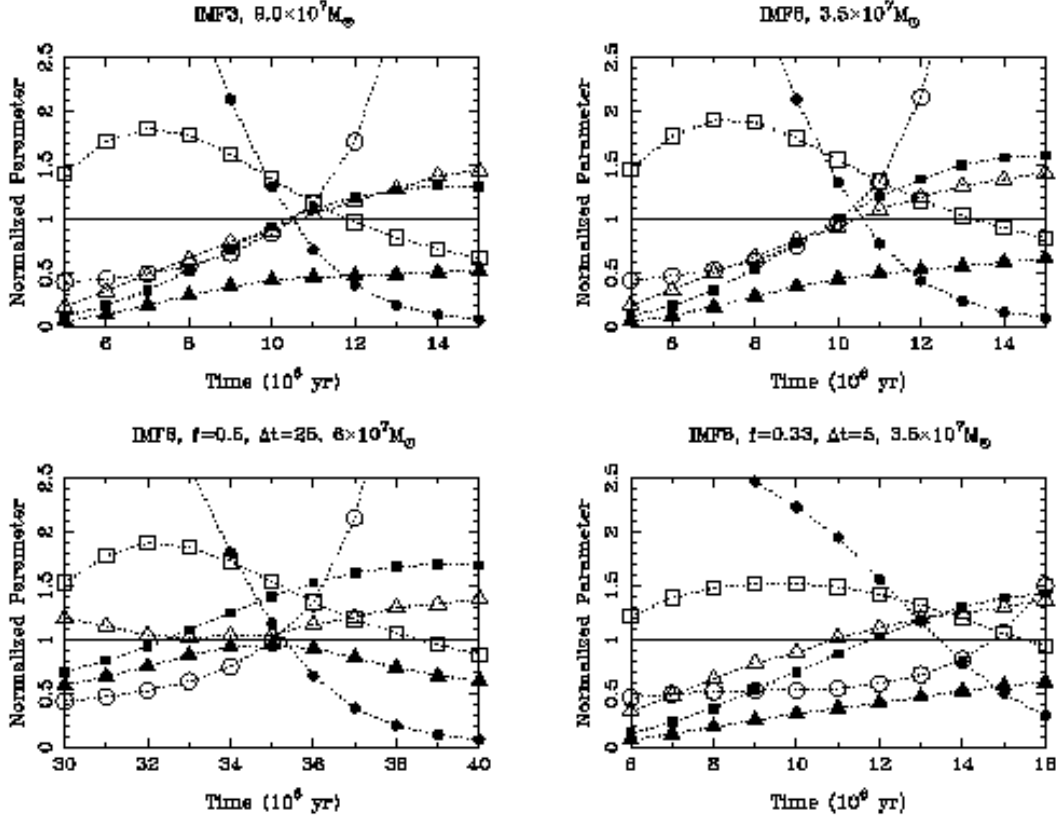


Fig. 13.— Starburst models of NGC 253 using a solar-neighborhood IMF (RLRT93’s IMF 3) and an IMF biased towards massive-star formation (RLRT93’s IMF 8). The points represent output from our starburst model as a function of time, where each curve has been ratioed to the corresponding observational parameter listed in Table 2. A reasonable fit is indicated where all the curves come within the range of uncertainties to match the target value (ideally at 1). The IMF used and the mass required to match the observations is indicated for each panel. For the bottom panels, double-burst models with a delay Δt (in millions of years) between bursts and the fraction f of the mass that was contained in the second burst are presented. The symbols represent the following quantities: open square = L_{Bol} , open triangle = CO index, open circle = $T(\text{UV})_{40}$, filled triangle = SN rate, filled square = L_K , filled circle = N_{Lyc} .

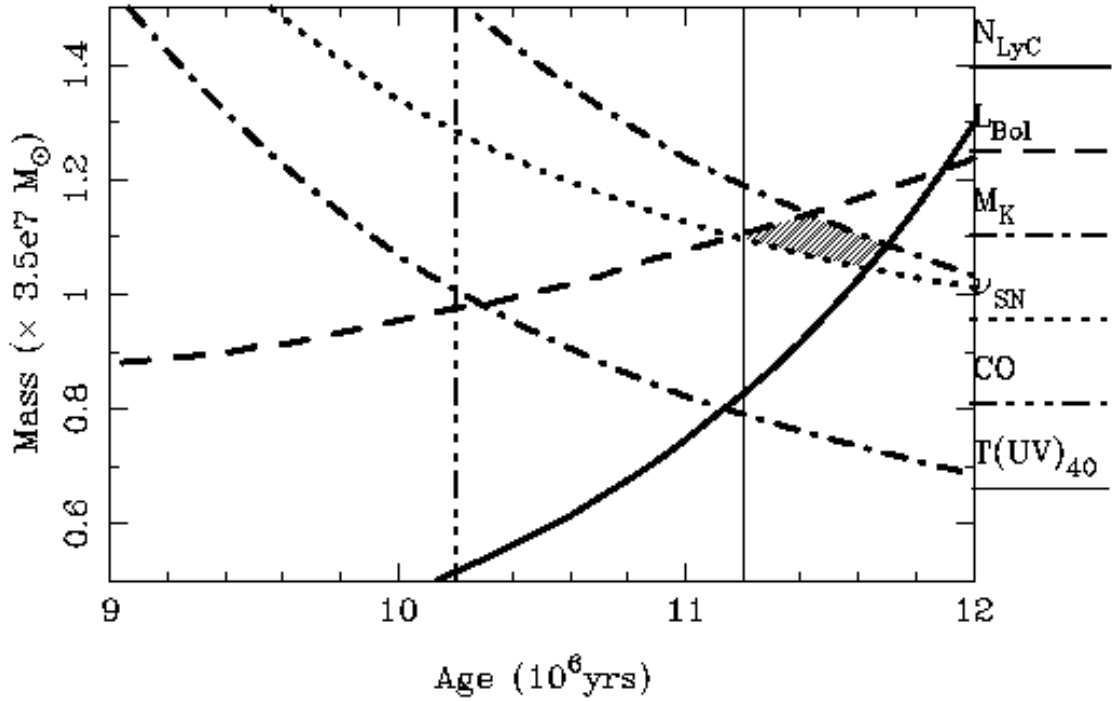


Fig. 14.— Allowed values in the (mass, age) plane for a single-burst starburst model using IMF8 of RLTLT93. The hatched region is constrained by the model values from Figure 13 with uncertainty ranges as described in the text. The CO index and $T(\text{UV})_{40}$ parameters do not scale with mass and therefore serve primarily as age constraints.